NUREG/CR-5126
SAND 88-1407

TAC2D Studies of Mark I Containment Drywall Shell Melt-Through

Prepared by J.J. Weingardt, K.D. Bergeron

Sandia National Laboratories

Prepared for
U.S. Nuclear Regulatory
Commission

NUREG/CR-5126
SAND88-1407
R4

TAC2D STUDIES OF MARK I CONTAINMENT DRYWELL SHELL MELT-THROUGH

Jay J. Weingardt*
Kenneth D. Bergeron

Manuscript Completed: May 1988
Date Issued: August 1988

Sandia National Laboratories
Albuquerque, NM 87185
Operated by
Sandia Corporation
for the
U.S. Department of Energy

Prepared for
Division of Reactor Accident Analysis
Office of Nuclear Regulatory Research
U.S. Nuclear Regulatory Commission
Washington, DC 20555
Under Memorandum of Understanding DOE 40-550-75
NRC FIN No. A1198, A1322

* Science Applications International Corporation
Albuquerque, NM
Contract No. 06-6990

ABSTRACT

A series of parametric calculations of the thermal attack of molten corium on a steel shell has been performed with the TAC2D computer code in order to elucidate uncertainties about the survivability of the BWR Mark I containment boundary in the event of a core-melt accident. Since TAC2D is a two-dimensional heat conduction code, it is not possible to capture some of the complexities of the corium spreading process or the debris-concrete interactions which would occur in this accident scenario. However, the two-dimensional transient nature of the thermal attack is modeled better with TAC2D than is possible with existing debris-concrete interaction codes. This study was therefore undertaken as a supplement to earlier work with debris-concrete interaction codes (like CORCON-MOD2), with the intention of assisting members of expert panels assessing uncertainty in severe accident phenomena for the US Nuclear Regulatory Commission's NUREG-1150 project. A total of 23 calculations are reported, consisting of two base cases (one with overlying water and one without) and numerous sensitivity variations about each case. The study is not intended as an uncertainty assessment per se, since the choice of parameters for the sensitivity variations is not intended to represent estimates of their ranges of uncertainty. Rather, it is intended that the results can be combined with assessments of the parameter ranges to assist in the estimation of overall uncertainty about the drywell shell melt-through issue. Sensitivities investigated include mixed versus layered corium, heat transfer parameters upward and downward, initial corium temperature, chemical heating rate, heat transfer conditions in the gap outside the shell, and corium depth. Most of the cases (21) resulted in ablation and melt-through of the shell in times that ranged from 8.3 minutes to 75.8 minutes. The two cases that did not melt both involved the mixed debris assumption and enhanced boiling heat transfer to an overlying water pool. A brief discussion is given of the limitations of the modeling and the various contributors to uncertainty, including those addressed by the study and those not addressed.

TABLE OF CONTENTS

Illustrations

TABLES

ACKNOWLEDGMENT

The supporting analysis of W. A. Gu to estimate the effective atmosphere emissivity (Appendix A) is gratefully acknowledged.

1.0 INTRODUCTION

In the event of a core melt-down and subsequent release of molten corium onto the drywell floor of a Boiling Water Reactor with a Mark I containment design, the issues of corium spreading to the steel drywell shell and thermal attack on the shell become extremely important. Numerous studies of the question have been undertaken, beginning with the analysis presented in Reference 1. In the draft version of the U.S. Nuclear Regulatory Commission's (USNRC) Risk Reference Document, NUREG-1150 [2], the drywell shell melt-through issue was identified as being one of the most important contributors to the uncertainty in risk for the Peach Bottom plant. For the final version of NUREG-1150, the issue is expected also to play an important role. Consequently, for the purpose of assisting the expert panels who will assess the uncertainty in this issue for NUREG-1150, a study was initiated specifically to address an important aspect of the problem--namely the transient conduction aspects of the steel shell attack.

Numerous phenomenological uncertainties affect the drywell shell melt-through issue. These include the amount, composition, and temperature of the debris penetrating the vessel and also the rate and extent of debris spreading (which may be influenced by the presence of water on the drywell floor). These corium spread uncertainties will not be addressed explicitly in this report. Instead, we focus on processes which occur once the debris makes contact with the shell.

The shell thermal attack issue detailed analysis of two- or three-dimensional transient debris-concrete interaction phenomena coupled with two- or three-dimensional transient heat transfer and conduction phenomena. No existing calculational tool can handle both aspects of the problem satisfactorily, though 2D codes exist which treat the uncoupled cases. In particular, the CORCON code [3] models the concrete ablation problem, including a broad range of chemical and physical models, but the heat conduction treatment is simplistic and generally unsuitable for the shell attack question. On the other hand, numerous 2D codes for transient heat conduction exist, but these are unsuited for the ablation and chemistry phenomena. This report presents the results of numerous calculations with a code of the latter variety, a heat conduction code called TAC2D. Since the study is restricted to the thermal attack question, with the issue of corium spreading relegated to other studies, the corium pool is assumed to be initially in contact with the shell, and an initial temperature of the pool is arbitrarily specified.

It should be emphasized at the outset that it was not the purpose of this study to bridge the gap between what is needed in analysis tools and what is available. Rather, the study was intended to provide the maximum amount of information (subject to the time limitations for the study) which could be generated with a standard heat conduction code as applied to the thermal attack question. The information is not, in fact, being presented as "best-estimate" analysis, since the debris-concrete interaction part of the problem would be much better treated with CORCON. It was hoped, however, that the sensitivities revealed in this pure conduction/heat transfer approach to the problem would be useful for assessing overall uncertainties. What the method lacks in mechanistic detail is to some extent made up for by the clarity of the approach and visibility of the assumptions.

This study was directly supported by the NUREG-1150 projects at Sandia, and this report is oriented towards the needs of the expert panel reviewing the issues as they appear in the NUREG-1150 Containment Event Tree for Peach

Bottom. The information in this report was delivered to the expert panel members in a letter report [2a] prior to their final elicitation. It should be understood that the schedule requirements of the panel precluded the implementation of more sophisticated models than those used here. Since the letter report was transmitted, a number of ideas about extensions or improvements of the calculational matrix have arisen, and it is anticipated that a future publication [2b] will explore these possibilities. The goal of the present report, however, is to formally document the material actually presented to the NUREG-1150 panel so that their uncertainty assessments can be viewed in the context of what was available to them at that time.

The remainder of this report is organized as follows: in Section 2, the basic TAC2D code is described, along with the nodalization used for the drywell geometry and a number of constitutive models which have been developed for this application; Section 3 provides results of a sensitivity study, where parameters have been varied over somewhat arbitrary ranges in order to determine the key sensitivities; Section 4 discusses these results in terms of what ranges those parameters might lie in, and what factors should be considered in assessing uncertainties; finally, Section 5 summarizes the results and indicates directions for future analyses.

2.0 MODEL DESCRIPTION

2.1 The TAC2D Code

The fundamental calculational tool utilized in this study was the TAC2D thermal analysis code [4]. TAC2D is a two-dimensional finite-difference conduction code developed by Gulf General Atomic. It is a generalized heat transfer code designed to model many of the transient thermal phenomena encountered in the nuclear industry. The two-dimensional cylindrical geometry package utilized here is only one of several geometric packages available. The dimensional nodalization capabilities are easily enhanced, but a matrix of 40 axial by 30 radial nodes proved to be sufficient for the Mark I shell geometry. Although the basic code package lacks models for many of the fundamental heat transfer phenomena encountered in this study, the versatility and relative computational speed of TAC2D provided the framework to implement numerous heat transfer models and to raise the code's sophistication to a level sufficient to perform these transient thermal calculations. Sections 2.2 and 2.3 describe the geometric and phenomenological models utilized in this study.

2.2 Geometric Models

A schematic drawing of the Mark I containment structure extracted from the draft version of NUREG-1150 [2] is shown in Figure 1. The region of greatest importance to the early shell melt-through issue is enclosed in the small rectangle. The rectangle has been reoriented so that the translated axes of the rectangle roughly coincide with the geometric boundaries available in the R-Z geometric package of TAC2D. An enlargement of the rectangular region is shown in Figure 2, which provides much more detailed information about the region of interest. Neither Figure 2 nor any of the other figures that follow it are drawn to scale. They are only intended to provide insight into the nodalization schemes utilized.

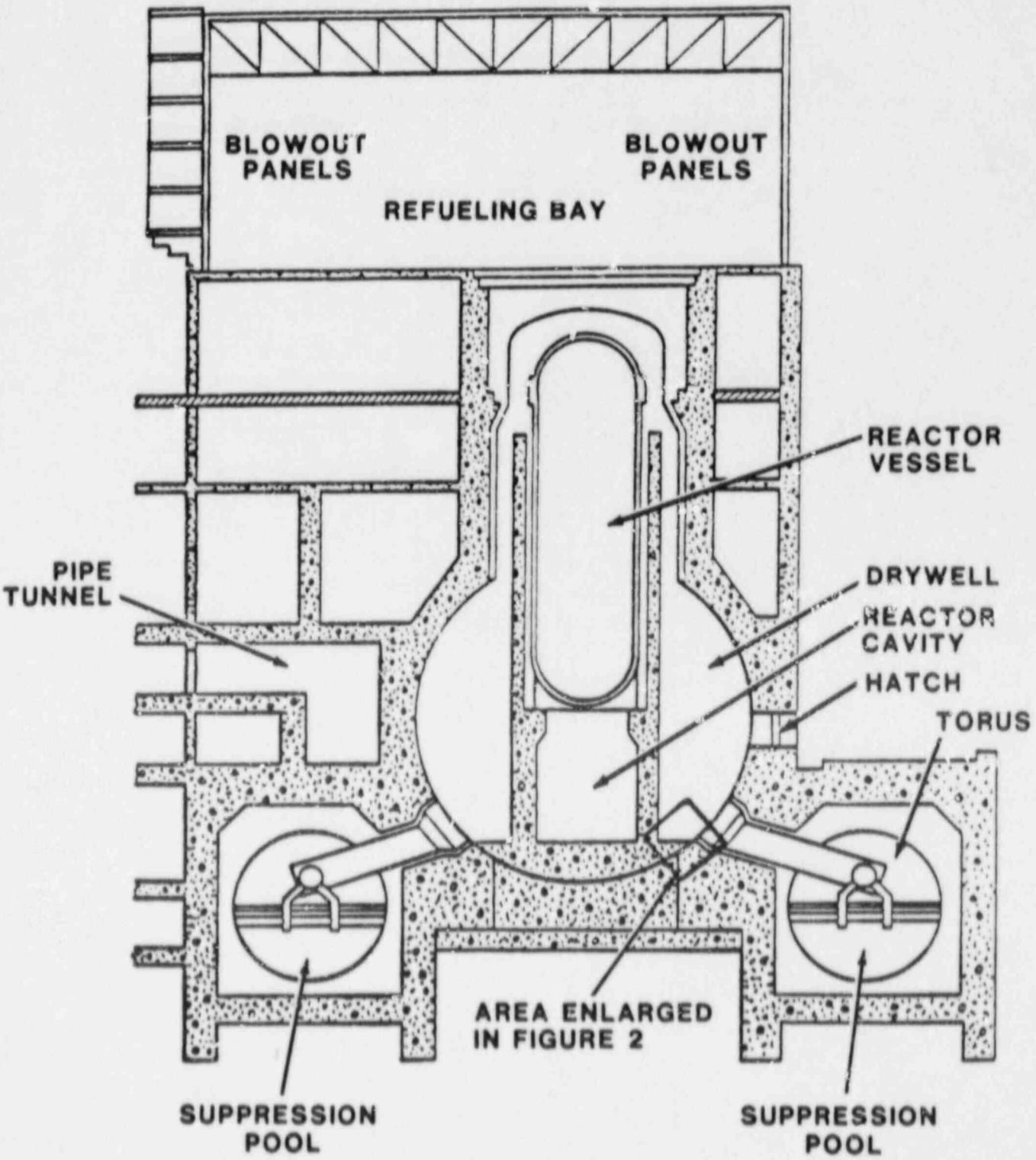

Figure 1. Containment Schematic for the Peach Bottom Mark I BWR (Reference 2)

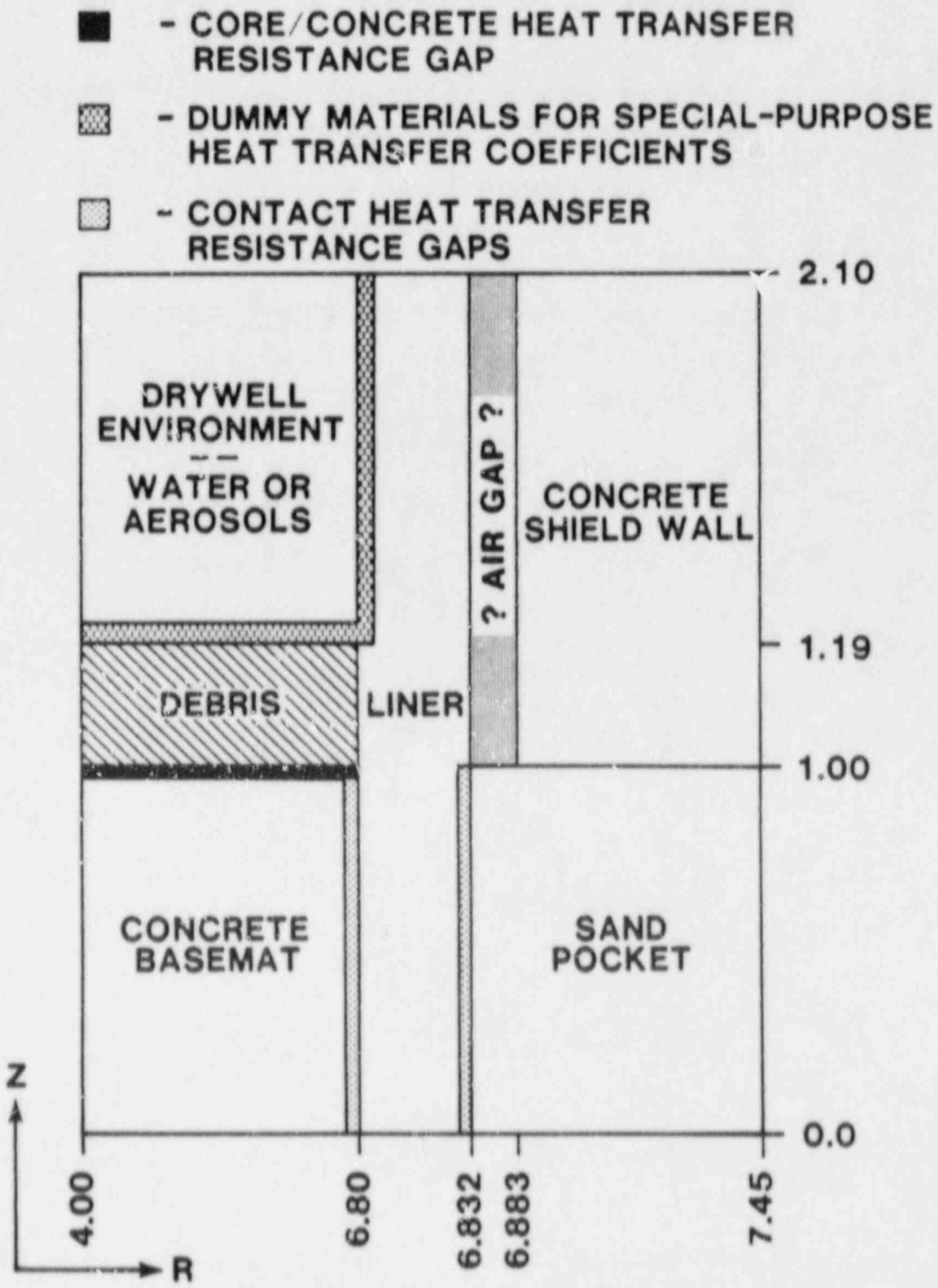

Figure 2. Mark I Drywell Geometry for the Shell Thermal Attack Calculations. Units are m.

Since the issue at hand is drywell shell survival, the most critical region of the problem is the carbon steel shell immediately adjacent to the debris. However, the geometric extent of the model goes well beyond this small critical region to include large volumes of concrete and sand which act as heat sinks. Massive volumes of heat sinks were included to adequately treat the thermal problem and to reduce dependency on ambiguous and ill-defined boundary conditions. Both the upper and lower horizontal boundaries as well as the outer radial boundary (at 7.45 m) are treated as constant temperature surfaces. Temperatures in the materials immediately adjacent to these surfaces remained at their initial values throughout each of the calculations, and the heat fluxes across the constant temperature boundaries were always negligible. Therefore, we can conclude that the volumes of heat sinks included in the geometric models were sufficient to completely isolate the critical region from the boundary conditions.

Contrary to the boundaries described above, the inside radial boundary (at 4.0 m) may be more closely coupled to the liner's thermal response. The inside radial boundary may play a more critical role in the calculation because the effective thermal conductivity of molten core debris can be much higher than the conductivity of either sand or concrete. The boundary is treated adiabatically to prevent unrealistic thermal losses across the surface and to provide a condition that allows us to assess the effect of the boundary on the results. In every calculation performed, the radial temperature gradient through the debris was very small near the inside radial boundary, indicating that a sufficient volume of debris was included to isolate the shell from that boundary.

The carbon steel shell is the single most important constituent of the geometry, and a more detailed description of its physical characteristics is warranted. Bechtel as-built drawings indicate that the shell is 2 cm (1.25 in) thick near the concrete basemat, and as Figure 1 indicates, the shell is spherical in this region. The carbon steel shell emerges from the floor of the containment building between the concrete and a sand pocket at roughly a 45° angle. The angle plays important roles in two aspects of the transient heat transfer problem. First, the slope of the shell will cause the length of the shell in contact with core debris to be roughly 40 percent greater than the average depth of debris on the drywell floor. Second, the angle of the shell affects the boiling heat transfer from the shell; this effect will be discussed later.

As Figure 2 indicates, heat transfer between the shell and the concrete floor and between the shell and the sand pocket has been limited through the use of heat transfer resistance gaps. Although heat losses to these two heat sinks were not expected to be significant, the gaps were included for completeness to model contact heat transfer resistances. The two regions are 0.5 mm gas-filled gaps that allow one-dimensional radiation and conduction heat transfer. Figure 2 also shows a core/concrete interaction heat transfer resistance gap between the debris and the concrete floor. The gap was included to provide a medium in which the downward heat flux from the debris to the basemat could be controlled to coincide with values typical of CORCON calculations.

The question marks (?) utilized in Figure 2 in the gap between the shell and the concrete shield wall were included to draw the reader's attention to the uncertainty surrounding the issue of the contents of the gap: is it an air gap, or is it filled with ethafoam insulation? The issue is discussed in Section 4.7.7 and will not be described in greater detail here. However, in the event that the gap contains only air, other questions

arise, such as whether or not high temperatures and high pressures have forced the shell to expand and come into contact with the concrete shield wall. Chicago Bridge and Iron (CB&I) performed a finite element structural analysis on the Mark I containment under the conditions described above [5]. The results indicate that at elevations well above the floor, the shell expands and comes into contact with the shield wall. However, the CB&I analysis also showed that the sand layer prevents the shell in close proximity to the basemat from expanding. Since the critical region of interest in the shell melt-through issue is directly above the sand pocket, the two-inch (5.1 cm) gap is maintained throughout these calculations.

The TAC2D geometric input utilizes a standard cylindrical finite-difference nodalization scheme. Figures 3 and 4 are detailed drawings of the two standard geometric models utilized. The drawings provide all of the important dimensions and finite-element structures. The two models were developed to treat different debris configurations. The model in Figure 3 was utilized for calculations that included well-mixed debris, whereas the model in Figure 4 was developed for calculations that included stratified layers of metallic and oxidic debris. In both cases, very fine radial nodes are utilized through the shell to provide detailed information about thermal gradients and temperature extremes. The inner and outer radial nodes in the shell are only 1 mm thick. These thin nodes are included to provide effective surface temperatures that are utilized in several of the more complex heat transfer models.

2.3 Specialized Thermal Models

2.3.1 Bulk Thermal Properties

Material mixtures of interest in the Peach Bottom Mark I drywell shell calculations include sand, limestone-concrete, carbon steel, and core debris. The overlying drywell environment referenced in Figure 2 contains either a saturated water pool or a gas atmosphere containing aerosols liberated by the core concrete interactions. In either case, the drywell environment is assumed to contain a constant temperature material. For the water case, the pool temperature was taken to be 373 K. For the aerosol case, CONTAIN [6] calculations performed at Oak Ridge National Laboratory indicate that gas temperatures within the containment building are about 1100 K at the time the debris comes into contact with the liner.

Thermophysical properties for the sand, concrete, and carbon steel were obtained from Reference 7 and were treated with temperature dependence to the extent that data were available. Thermophysical debris properties were defined as the volume-weighted average of the individual constituent thermophysical properties. Individual constituent properties were once again obtained from Reference 7. Appendix B gives quantitative details of the individual component properties. The core debris is broken down by its constituents in Table 1 [8]. One of the most important parameters studied in the sensitivity analysis was the effect of convection and boiling on the effective debris thermal conductivity. Convective flow of the liquid debris and gas sparging through the debris can alter the effective thermal conductivity dramatically. Sensitivity calculations were performed by applying a multiplier to the solid conductivity that ranged from a value of 2.0 (a 100 percent enhancement) to 10.0 (a 1000 percent enhancement). The impact of this alteration is described in Section 4.2.3. We should note that the multipliers described here are maintained throughout each calculation regardless of debris temperature. A number of difficulties associated

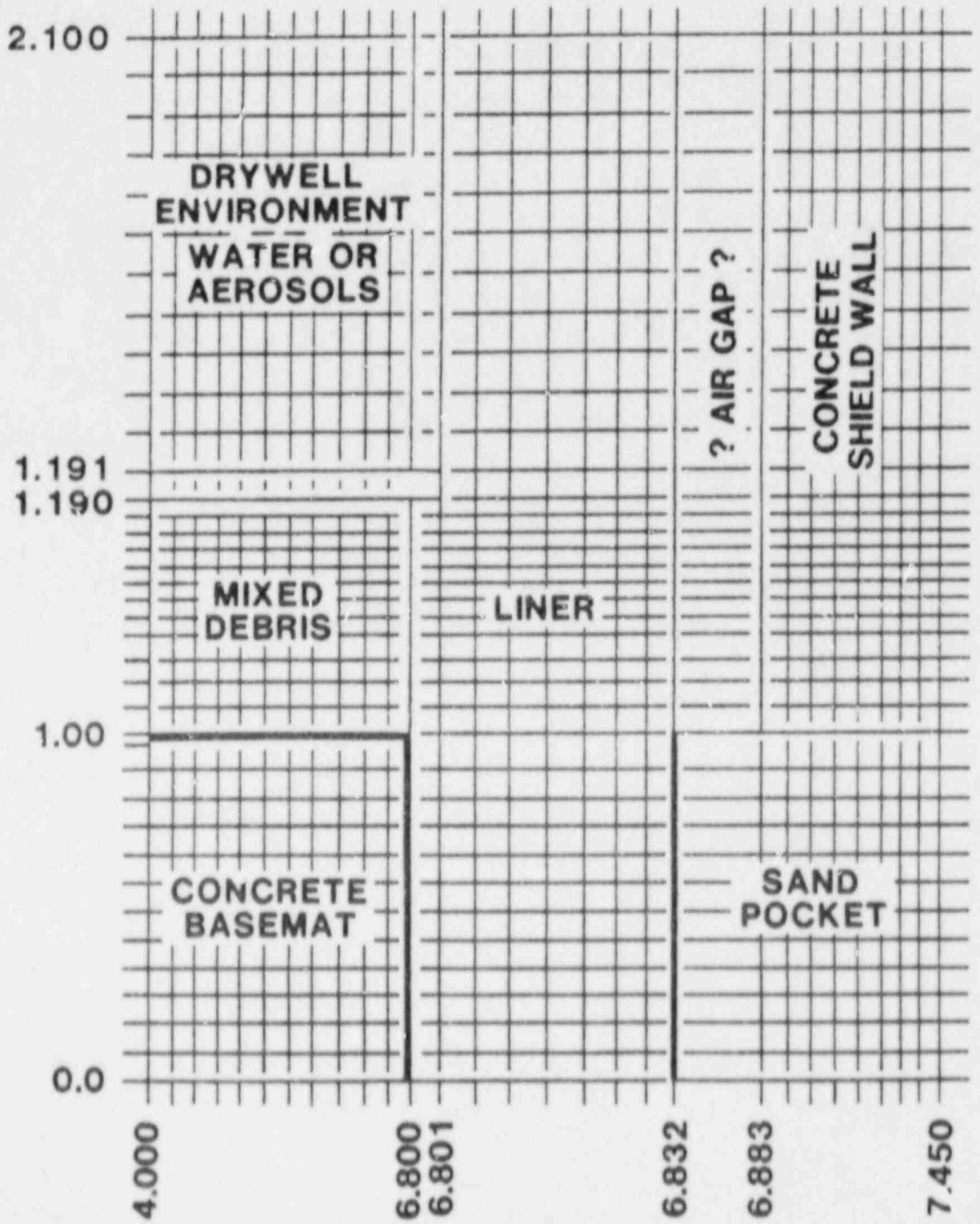

Figure 3. Nodalization for the Mixed Debris

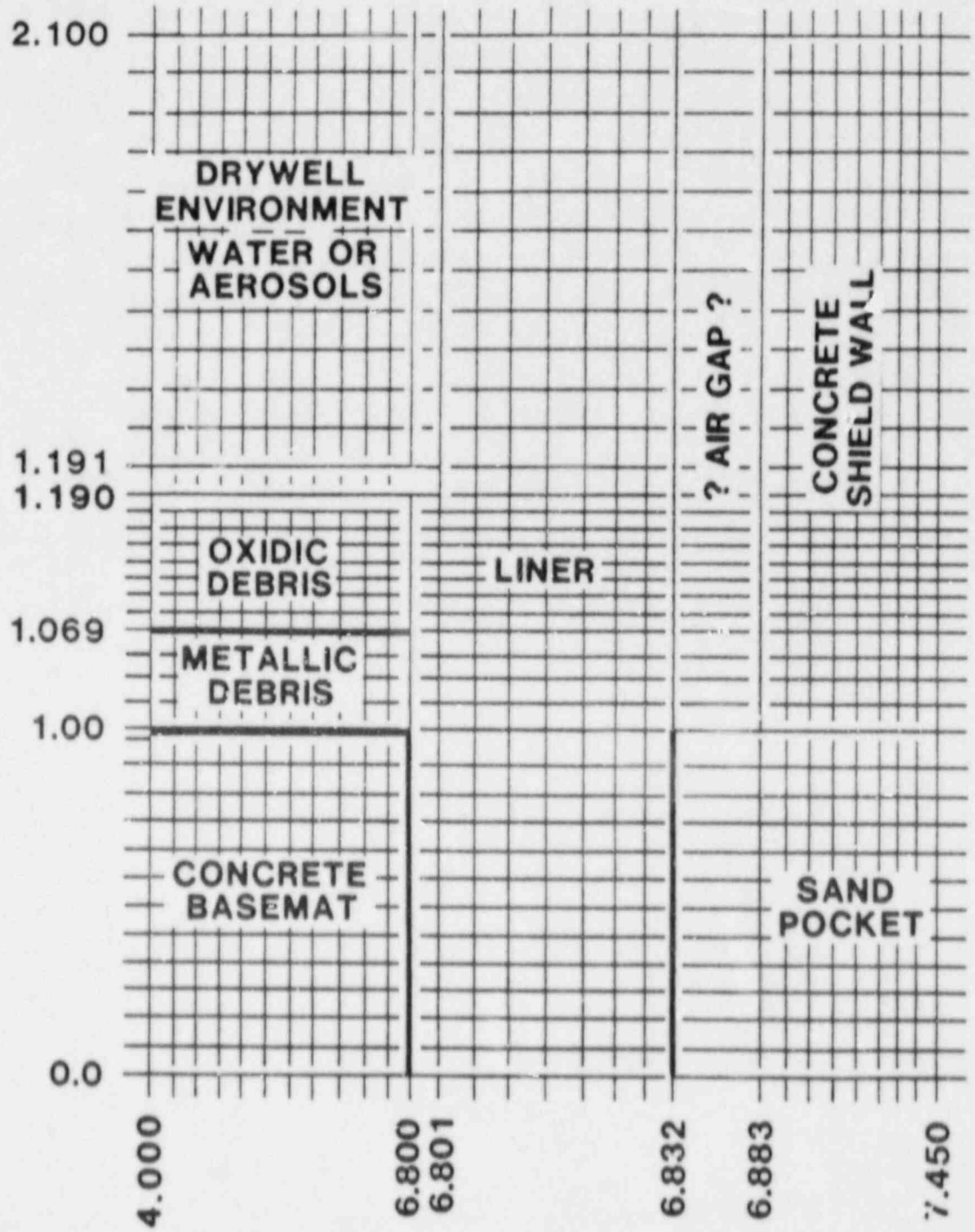

Figure 4. Nodalization for the Layered Debris

Table 1

Debris Composition Corresponding to 100 Percent of the Peach Bottom Core Inventory [8]

Component	Mass	Density 10^3Kg/m^3	Volume Fraction	Mass Fraction
UO_2	159,413	10.96	0.416	0.541
ZrO_2	41,624	5.60	0.213	0.141
FeO	1,564	5.18	0.009	0.005
Fe	45,986	7.86	0.167	0.156
Zr	34,677	6.50	0.153	0.118
Cr	7,397	7.19	0.029	0.025
Ni	4,110	8.90	0.013	0.014
	294,771		1.000	1.000

Volume Fraction of Metallic Components = 0.363

Mass Fraction of Metallic Components = 0.313

with this approach to the combined fluid motion/ heat conduction problem are discussed in Section 4.

2.3.2 Shell/Concrete Shield Wall Gap

As mentioned earlier, the material in the gap between the shell and the concrete shield wall might be air, ethafoam insulation, or some spatially dependent combination of the two. Although the gap's contents are uncertain, it is convenient and fairly accurate to assign the region a very low specific heat which was utilized for all calculations regardless of the material that was assumed to reside in the gap. The heat transfer, on the other hand, varies dramatically depending on the gap material. For the foam insulation case, a thermal conductivity of 0.024 W/m-K was assumed which is typical of polyurethane foams; it does not vary with temperature in our model. For the air case, combined convection and radiative heat transfer is defined by:

$$h_{gap} = h_{convection} + h_{radiation}. \quad (1)$$

Convective heat transfer coefficients are assumed to vary linearly with the internal gap temperature from 1.0 to 10.0 W/m^2-K over a range of 300 to 1500 K as follows:

$$h_{convection} = 7.5e\text{-}7 * T - 1.25e\text{-}4. \quad (2)$$

This treatment was intended to capture the expected slow increase in heat transfer coefficient with increasing temperature, but in fact the temperature dependence was not an important issue since preliminary calculations indicate that air gap conductance is dominated by radiative heat transfer which is given by [9]:

$$h_{radiation} = \frac{\sigma \left(T_b^4 - T_c^4 \right) / \left(T_b - T_c \right)}{\frac{1}{\epsilon_s} + \frac{1}{\epsilon_c} - 1.0} \quad (3)$$

where

T_b = shell back side surface temperature (K),

T_c = concrete surface temperature (K),

σ = Stephan-Boltzmann Constant = 5.67e-8 $W/m^2 \cdot K^4$,

ϵ_s = carbon steel emissivity, and

ϵ_c = concrete emissivity.

The effective gap thermal conductivity can then be determined by:

$$K_{gap} = h_{gap} \Delta r, \quad (4)$$

where Δr is the gap thickness.

The two surface temperatures are continuously evaluated within the code, and the steel emissivity is assumed constant at 0.64. The concrete emissivity, however, is not well known and may vary strongly with temperature (see Section 4). In addition, the emissivity of the concrete shield wall may also be sensitive to the method that was utilized to remove the ethafoam insulation 13 years ago. Therefore, given the large range of possible values, the concrete emissivity will be one of the parameters varied in the sensitivity analysis.

2.3.3 Boiling Heat Transfer Models

In the event that the drywell is flooded, boiling heat transfer will play an important role in the transient analysis. Figure 5 shows a standard heat flux controlled boiling curve. Both surfaces of interest in the Mark I shell calculations (the horizontal debris surface and the inclined shell surface) are assumed to be heat flux controlled. Boiling models are included for the stable film and nucleate boiling regions identified in Figure 5.

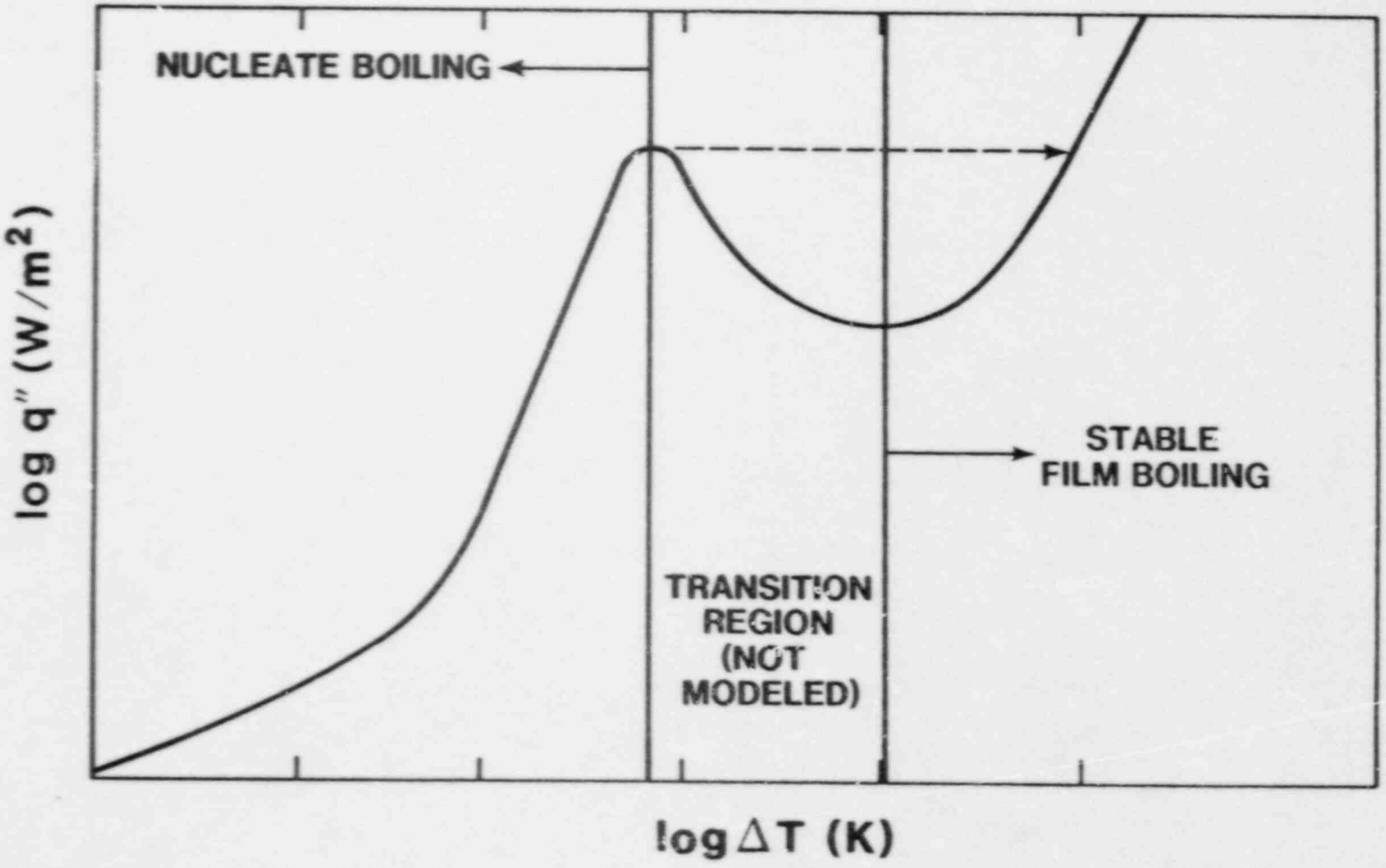

Figure 5. Boiling Regimes

2.3.3.1 The Debris/Water Interface

The extremely high temperatures coupled with internal heat generation in the debris forces heat transfer between the debris and the water into the film boiling regime. Once film boiling is achieved, this analysis does not allow transition back to stable nucleate boiling. The horizontal film boiling model is based on a correlation from Berenson [10]:

$$h = 0.425 \left[\frac{k_v^3 \, g \, h'_{fg} \, (\rho_\ell - \rho_v) \, \rho_v}{\mu_v \, (T_w - T_{sat}) \, \lambda_c} \right]^{1/4} \tag{5}$$

where

$$h'_{fg} = h_{fg} \left[1.0 + 0.5 \, \frac{C_{pv} \, (T_w - T_{sat})}{h_{fg}} \right], \tag{6}$$

and λ_c is the characteristic length which, in this case, is the bubble diameter given by:

$$\lambda_c = \frac{\sigma_{fg}}{g \, (\rho_\ell - \rho_v)}. \tag{7}$$

The individual parameters in equations 5, 6, and 7 are defined below:

h = heat transfer coefficient ($W/m^2 \cdot K$),

k_v = vapor thermal conductivity ($W/m \cdot K$),

g = acceleration due to gravity (m/s^2),

h_{fg} = latent heat of vaporization for water (J/Kg),

C_{pv} = specific heat of the vapor (J/Kg),

T_w = debris surface temperature (K),

T_{sat} = saturation temperature (assumed 0.1 MPa) (K),

ρ_ℓ = liquid density (Kg/m^3),

ρ_v = vapor density (Kg/m^3),

μ_v = vapor viscosity (poise), and

σ_{fg} = liquid surface tension (N/m).

Equation 5 describes the heat transfer coefficient for pool boiling from a solid surface. However, this basic model fails to capture some of the complex effects resulting from the molten core/concrete interactions. For example, molten core/concrete interactions generate large quantities of gases that subsequently sparge up through the debris and into the overlying water pool. Vigorous gas sparging may tend to break up the stable film boiling and enhance the overall heat transfer coefficient. Greene identified and quantified the effect of gas sparging on the heat transfer coefficient in liquid-liquid film boiling. He observed heat fluxes as much as six times larger than those predicted by Berenson's model for very vigorous gas sparging. However, Green's experiments to date have involved liquid-liquid interfaces, and most of the calculations performed here involve solid-liquid interfaces. Therefore, the direct application of Green's enhancement is not clear, and we therefore will use a multiplier on the boiling heat trarsfer coefficient as a sensitivity parameter.

2.3.3.2 The Shell/Water Interface

Immediately before debris comes into contact with the shell, the shell is assumed to be at 373 K. Therefore, at the beginning of the transient calculations, the boiling model calculates heat transfer coefficients from Rohsenow's nucleate boiling correlation [12]:

$$h = \frac{4.148e5}{(T_w - T_{sat})} \left[\frac{C_{pf} (T_w - T_{sat})}{h_{fg} Pr_f^{1.7}} \right]^{3.0303} \left[\frac{\mu_f h_{fg}}{\lambda_c^{1/2}} \right], \qquad (8)$$

where

C_{pf} = specific heat of the liquid (J/Kg),

μ_f = fluid viscosity (poise), and

Pr_f = fluid Prandtl number (dimensionless).

The parameters in Equation 8 that are not defined above were defined in Section 2.3.3.1.

The total heat flux (in W/m^2) from the shell to the water is given by:

$$q = h (T_w - T_{sat}). \qquad (9)$$

A correlation for the maximum nucleate boiling heat flux developed by Zuber [13] is utilized to determine the critical heat flux,

$$q_{crit} = 0.135\, h_{fg} \rho_v \left[\frac{\sigma_{fg}\, g\, (\rho_f - \rho_v)}{\rho_v^2} \right]^{1/4}. \qquad (10)$$

After the local nucleate boiling heat flux at any location along the steel shell exceeds the critical heat flux, the heat transfer coefficient is then calculated from the shell film boiling models. The boiling model does not

allow transition back to nucleate boiling after the critical heat flux has been reached.

Film boiling along the shell (which actually has a 45° slope as described earlier) is described by the average of Berenson's horizontal film boiling model given in Equation 3 and Bromley's vertical film boiling model [14]:

$$h = 0.943 \left[\frac{k_v^3 \, h'_{fg} \, (\rho_\ell - \rho_v) \, \rho_v}{\mu_v \, (T_w - T_{sat}) \, L} \right]^{1/4} , \qquad (11)$$

where L is a characteristic length which is assigned a somewhat arbitrary value of 0.5m. Local heat transfer coefficients are calculated at each interface node, and the heat flux is evaluated based on the local coefficient. Therefore, the boiling regime is independently selected in every node along the liner/water interface. This approach allows the code to apply discrete, localized heat transfer coefficients rather than broad-based average coefficients that might mask important phenomena.

2.3.4 Radiation Models for the Drywell Environment

In the event that the drywell is not flooded, the aerosols generated by the debris concrete interaction quickly fill the drywell. These aerosols provide a relatively opaque atmosphere to which the debris surface radiates. Section 2.3.1 described the basis for treating the environment as a constant temperature material. The same radiation heat transfer model is utilized here that was utilized for heat transfer across the shell/shield wall gap. The radiative heat transfer coefficients are applied in thin (1 mm) gaps between the debris and the aerosols as well as between the shell and the aerosols. These thin gaps were identified in Figure 2 as the "dummy materials for special purpose heat transfer coefficients." The debris and steel emissivities were assumed constant at 0.80 and 0.64, respectively, and the aerosol emissivity was calculated to be roughly 0.7 (see Appendix A).

2.3.5 Steel Ablation Treatment

The last major code modification implemented for the Mark I calculations was the steel ablation model. Without an effective ablation model, components of the liner that have melted would be left in place and effectively insulate the remaining solid portions of the liner. The ablation model applied here simply replaces molten steel with core debris. After a steel node is melted (which occurs at 1763 K), core debris is adiabatically moved into the node, and the molten steel is removed. By replacing molten steel with debris, materials with enhanced conductivities and volumetric heat generation are moved into contact with any shell structure that has not melted.

3.0 RESULTS OF SENSITIVITY STUDY

The approach used in this study was to define two "base cases," and then perform one-at-a-time sensitivity variations on nine key parameters. The two base cases differed only in that one corresponded to a dry atmosphere laden with aerosols, and the other corresponded to a water pool overlying the corium. The choices of the parameters for the base cases were not

intended to represent best estimates, but they are expected to be representative values. Some attempt was made to keep the base cases from being overly pessimistic (conservative) or optimistic (non-conservative), but the reader should be reminded that the principal goal was to observe how output quantities change with nominal changes in parameters, and not to take a position about what the range of the parameters might be. Thus, one should not directly infer the total range of uncertainty in output results from the sensitivity study. It was hoped, however that these results would be useful to the expert panel members whose task it is to assess the uncertainties.

3.1 Specifications of Sensitivity Parameters

A brief explanation of each of the parameters varied is provided below to help the reader evaluate the results. More extensive discussion of the uncertainties in the parameters will be found in Section 4.

DRYWELL ENVIRONMENT - The type of material present in the drywell with which the debris and the shell interact thermally. Both a flooded (H_2O) environment and a core/concrete aerosol (DRY) environment have been postulated.

CONDUCTIVITY ENHANCEMENT - A multiplier applied to the mass-averaged solid thermal conductivity of the mixed debris or the metallic debris layer. The conductivity of the oxidic debris in the stratified layer configuration is always treated with unenhanced thermal conductivity values. The multiplier is intended to represent enhanced heat transport due to fluid motion.

DEBRIS CONFIGURATION - The type of configuration the debris has settled into. It is uncertain whether the core debris can exist on the concrete floor in well-mixed (MIX) or layered (LAY) configurations. For layered configurations, the metallic components reside beneath the oxidic components.

CHEMICAL HEAT GENERATION - A multiplier applied to the volumetric heat generation term of the metallic component of the mixed debris and the metallic layer of the stratified debris. The multiplier represents the total chemical heat generation from oxidation reactions within the metallic debris components relative to the total decay heat generation. Decay heat generation is assumed to be 90 W/Kg of UO_2 which corresponds to the rather late melt release study in [6]. All of the decay heat generation occurs in the oxidic debris, while all of the heat generation resulting from oxidation reactions occurs in the metallic debris.

SURFACE CONTACT DEPTH - Debris depth in contact with the steel shell. A depth of 0.19 m roughly corresponds to 50 percent of the total core inventory if the debris is assumed to be 40 percent porous and uniformly spread over the drywell floor. A depth of 0.38 m corresponds to 100 percent of the core inventory. (Recall from Section 2.2 that the angled Mark I wall has been replaced in these calculations by a vertical wall.)

GAP CONDUCTION MODEL - The gap conduction parameter dictates the conductivity model used in the shell/shield wall gap based on the type of material that is assumed to fill the gap. Section 2.2 indicated that the gap was either filled with Ethafoam insulation which results in the use of a conduction model (COND) or air which results in the use of a radiation model (RAD).

CONCRETE EMISSIVITY - The emissivity of the surface of the concrete shield wall, ϵ_c, as used in Equation 3.

BOILING ENHANCEMENT - A multiplier on the flat plate pool boiling heat transfer coefficient representing enhanced heat transfer to the overlying water pool due to gas sparging or liquid-liquid contact.

INITIAL DEBRIS TEMPERATURE - The temperature of the debris pool at the start of the problem.

DEBRIS-CONCRETE HEAT TRANSFER COEFFICIENT - The heat transfer coefficient h_c between the bottom node of the debris and the top node of the concrete floor.

3.2 Discussion of Typical Results

In the next section, results from 23 TAC2D calculations will be summarized, but first, we will provide more detailed information about selected cases. Table 2 shows the values used for all the sensitivity parameters in the base cases. We will first consider the dry base case, designated D1. Figures 6, 7, and 8 give key results for this case. Most of the sensitivity variations gave results which qualitatively resemble the base case. The shell melted through in this case at about 15 minutes from the problem start. Figure 7 shows the radial temperature profiles at t = 1000 sec, shortly before shell melt-through. The first material radial node is at 4.45 m. One interesting point about this figure is that there is a broad temperature drop in the metal layer (top trace) between 6.25 m and 6.80 m. This is a conduction boundary layer caused by the cooling at the shell surface.

Figure 7 shows the axial temperature profile in the shell region just before melt-through occurs. Most of the shell is melted through at this time (exceeds 1763 K). Figure 8 shows the temperature histories at key locations in the system. The bulk metal layer temperature (top curve) steadily increases in time, while the front shell surface (triangles) follows the metal temperature with an offset corresponding to the thermal boundary layer seen in Figure 6.

A general picture that emerges from the sensitivity studies is that the shell does not begin to melt until the bulk metal temperature rises to a point that its temperature exceeds the melting point of the shell plus the temperature drop across the conduction boundary layer. Thus, if the rise in the bulk debris temperature is slow, shell ablation begins at a later time. This is seen in Figure 9, corresponding to case D4, which is a sensitivity variation corresponding to a much lower (by a factor of 3.5) chemical energy production rate in the metal layer. The metal temperature actually drops initially, but then turns around as the materials in contact with it heat up. The bulk metal temperature rise is much slower, but it continues to increase, and the shell inner temperature tracks it with an offset which is very similar to that observed in D1. The shell is melted through at 55.0 minutes (3300 sec) compared to 15.3 minutes in the base case.

Figure 10 shows that the corium heatup rate is relatively insensitive to conditions on the back side of the shell. This result corresponds to case D7, in which the air gap is replaced by an insulating material. The bulk metal temperature trace is virtually identical to that seen in Figure 8.

Table 2

Base Case Parameters

Parameter	Symbol	Value
Conductivity Enhancement	K^*	10.0
Debris Configuration	D.C.	LAY
Chemical Heat Ratio	Q^*	7.0
Boiling Enhancement	h^*	1.0
Concrete Emissivity	ϵ_c	0.70
Initial Debris Temperature	T_D^o	1825 K
Gap Conduction Model	Gap	RAD
Surface Contact Depth	L	0.19 m
Debris-concrete Heat Transfer Coefficient	h_c	800 W/m^2K

The inside shell surface temperature is also very little affected, but the back surface rises much more rapidly, and ablation occurs more quickly. The melt-through therefore occurs two minutes earlier (13.2 minutes) than in the base case.

The wet base case (W1) results are shown in Figures 11 through 13, which correspond to Figures 6 through 8 for the dry base case. The effect of the overlying water is very small, principally because of the fact that the overlying oxide layer in the mixed configuration tends to insulate the metal from the effect of the water. The temperature histories of the metallic and oxidic layers shown in Figure 13 are virtually indistinguishable from those of the dry base case shown in Figure 8. The main differences observed have to do with the shell temperatures at and above the level of the oxide layer (compare Figures 12 and 7 for heights greater than about 110 cm). Melt-through occurs at essentially the same time as in the dry base case.

In case W3, illustrated in Figure 14, we see a qualitatively different picture. Here, we have invoked the mixed debris option, and multiplied the boiling heat transfer coefficient by a factor of 6. The combination of these changes has the effect of cooling the corium (top curve) rather than

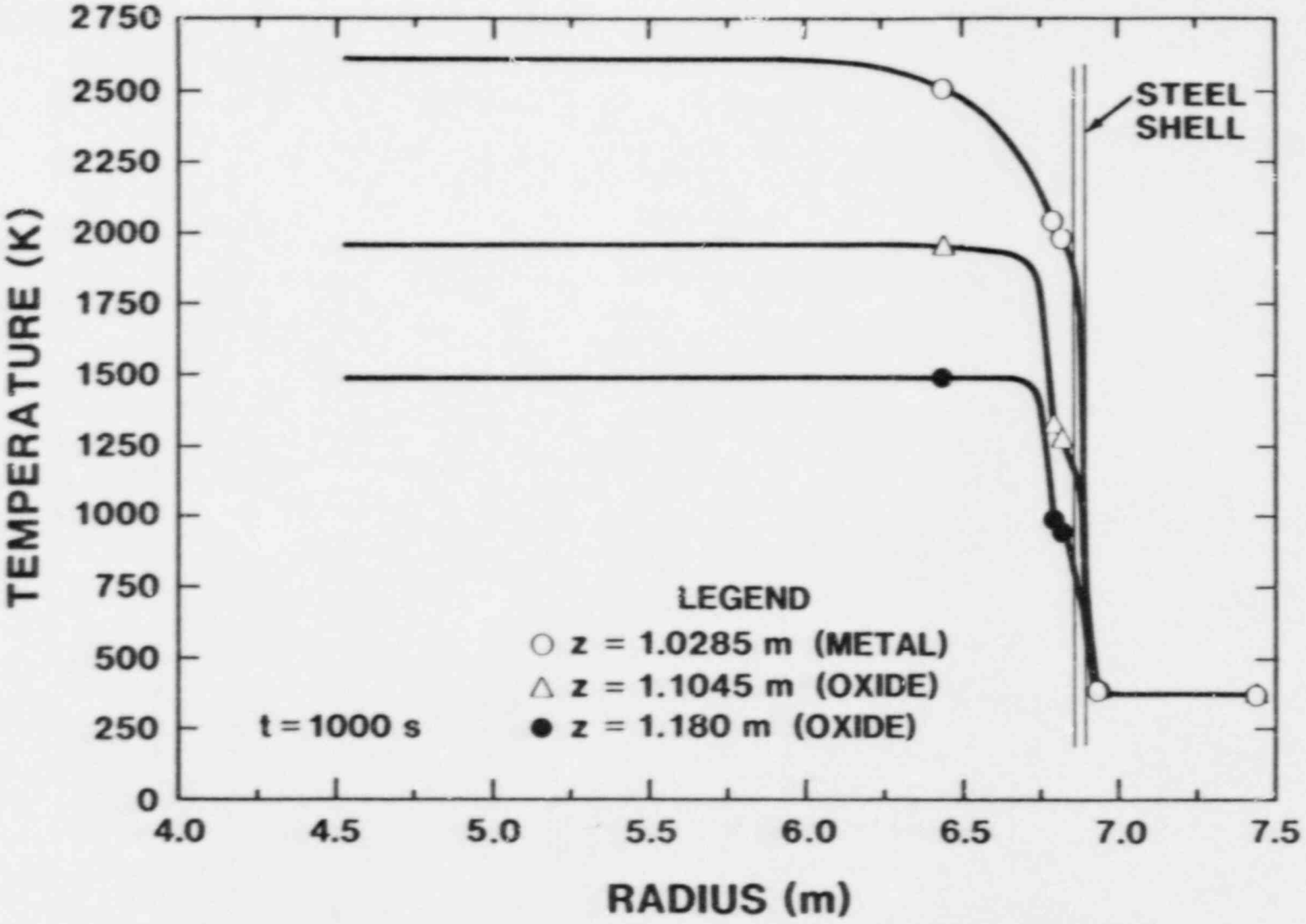

Figure 6. Temperature Profiles as a Function of Radius at t = 1000 Sec for the Dry Base Case (D1). Four traces corresponding to different vertical positions are shown. The top curve is near the bottom of the metal layer. Note the rather broad conduction boundary layer from about r = 625 cm to the shell at 680 cm.

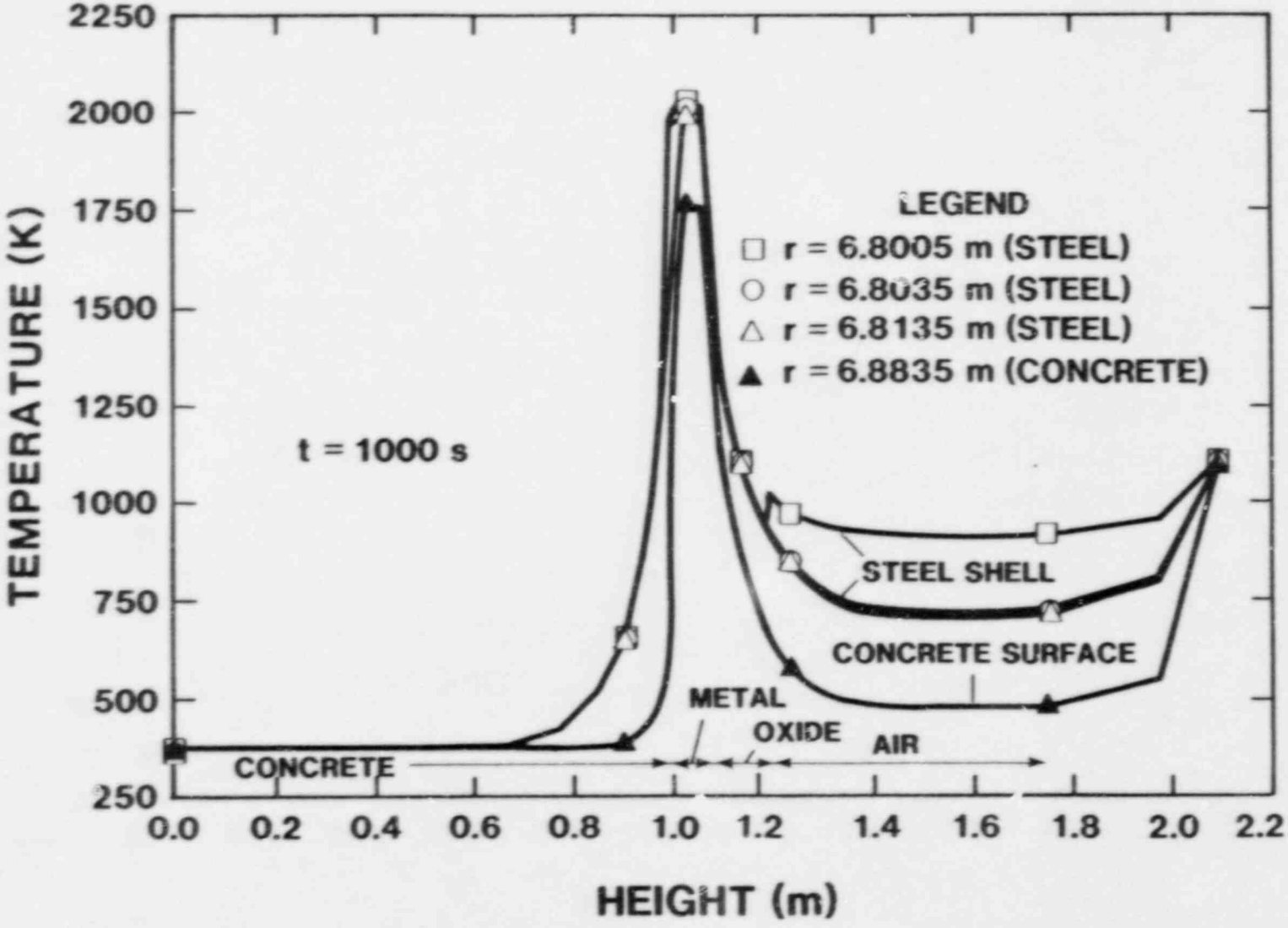

Figure 7. Vertical Temperature Profiles in the Shell Region for the Dry Base Case (D1). The lowest curve is surface temperature in the first concrete wall node, while the others are in the steel shell. Positions of the layers in the bulk region ($r < 680$) are indicated at bottom.

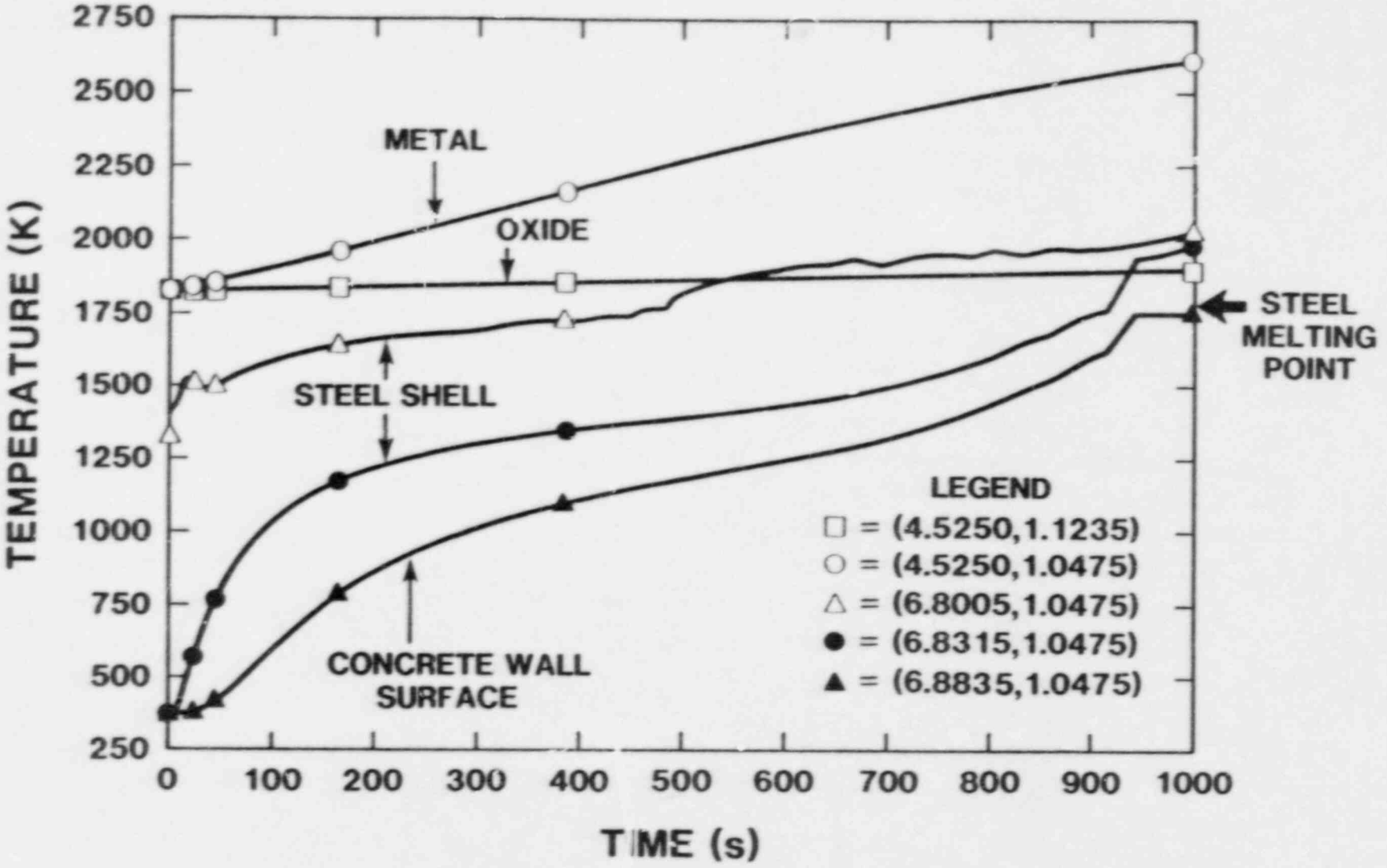

Figure 8. Temperature Histories for the Dry Base Case (D1). Five traces are shown. They correspond to the hottest node in each of the following: □ - oxide layer; ○ - metal layer, △ - inner surface of shell; ● - outer surface of shell; ▲ - concrete wall surface. The assumed melting point of steel is marked with an arrow on the right side of the figure.

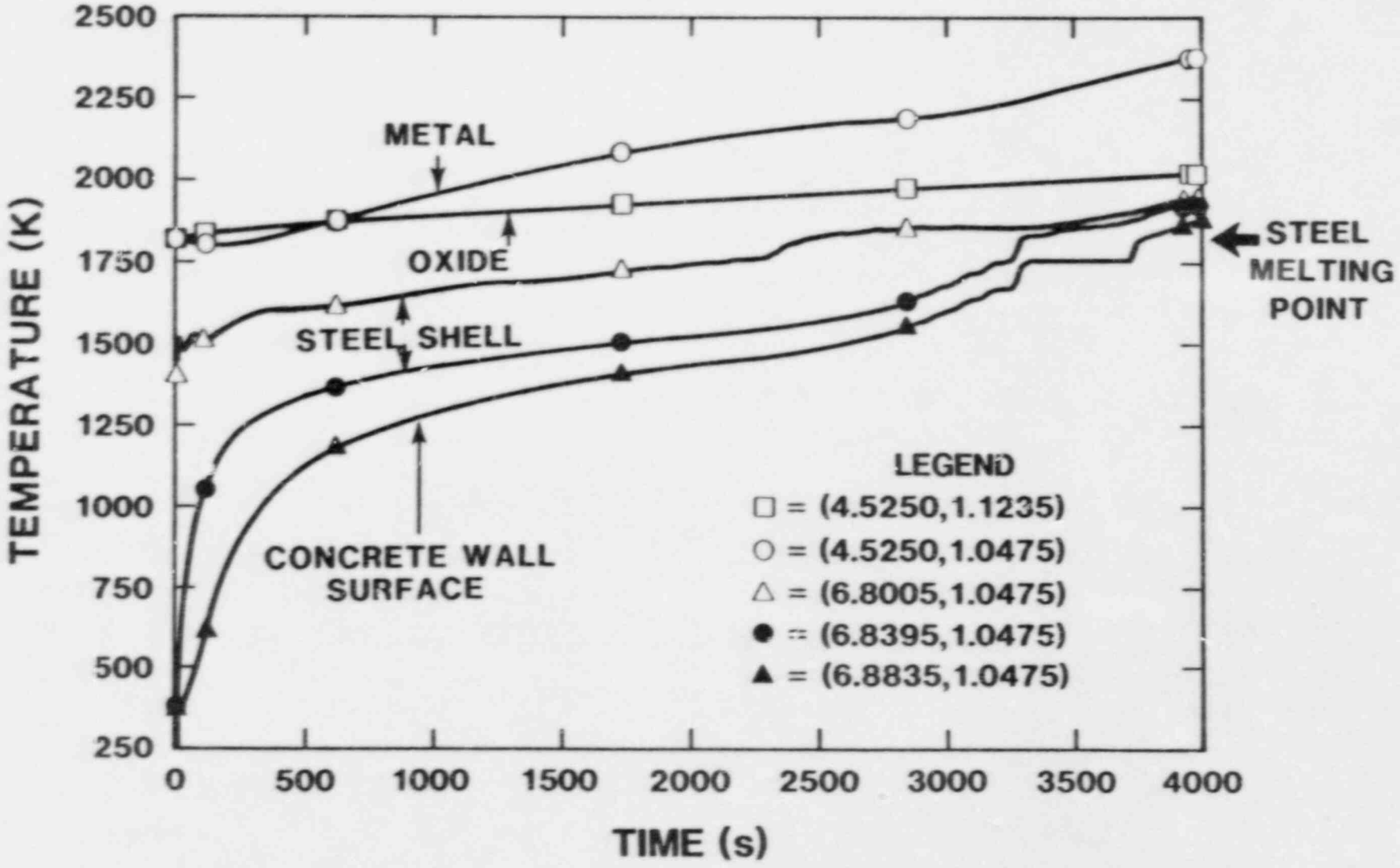

Figure 9. Same as Figure 8, but for Case D4 Which Has the Lower Chemical Heat Generation Rate (Q* = 2.0)

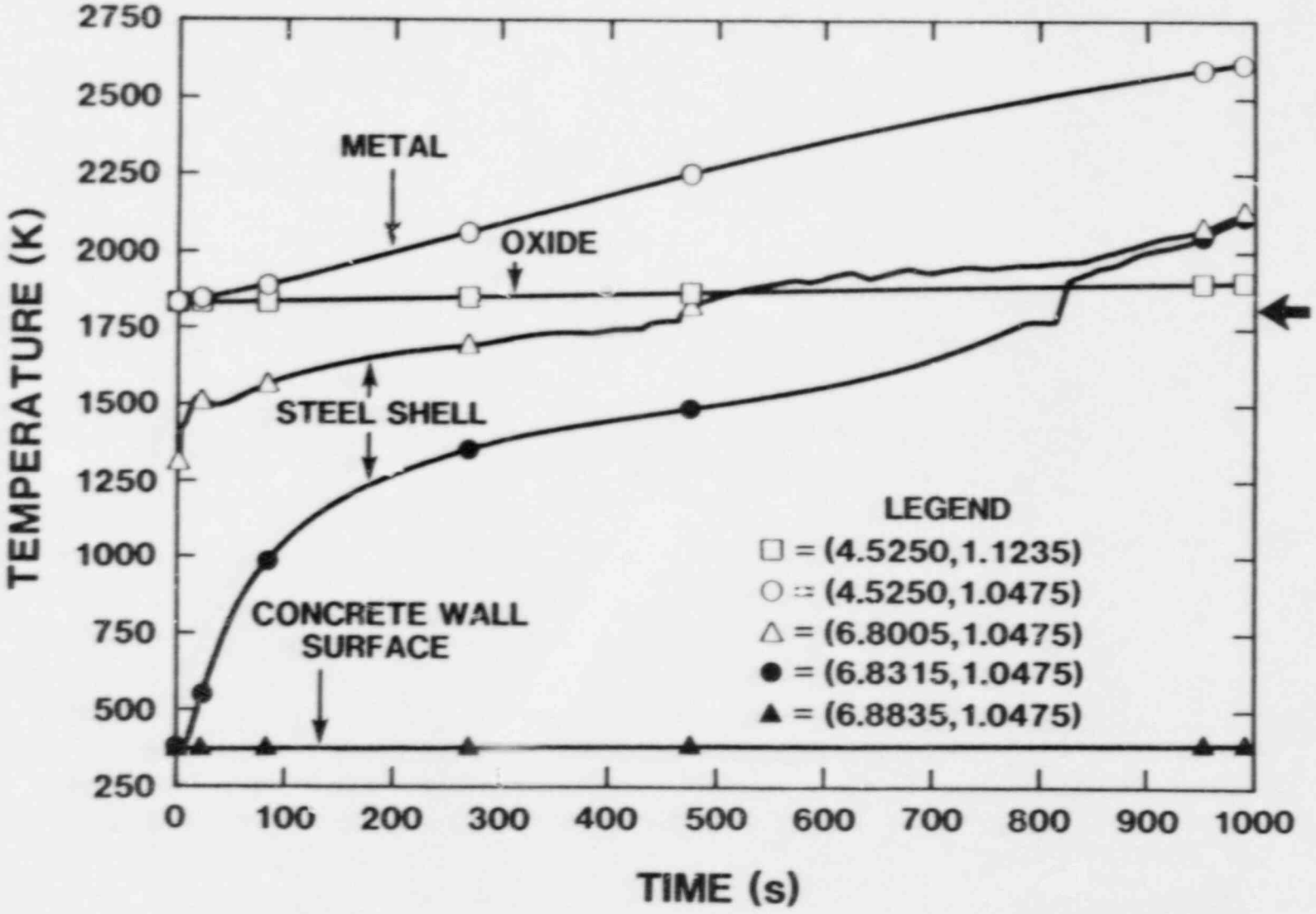

Figure 10. Same as Figure 8, but for Case D7, Which Has Insulation in the Gap

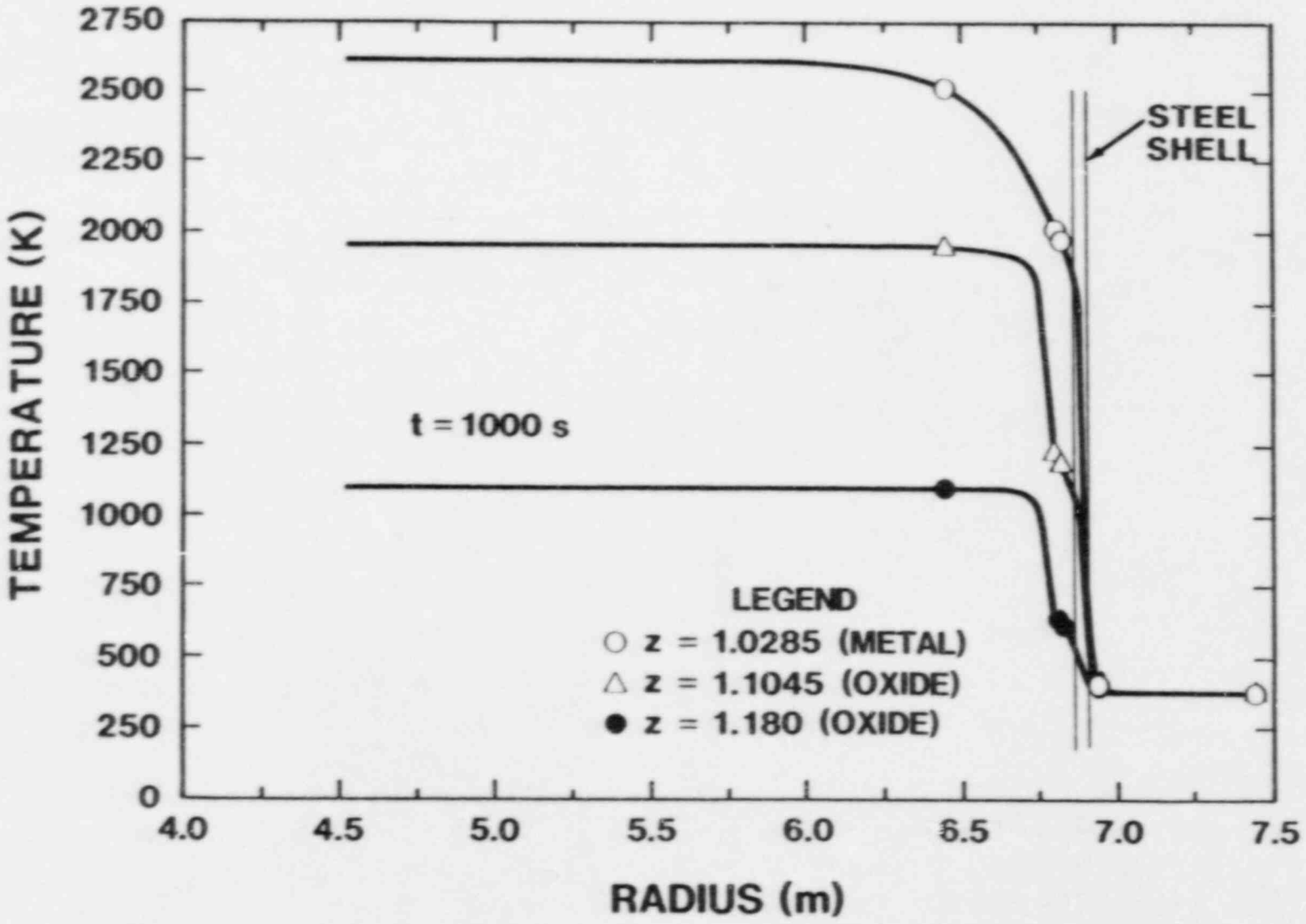

Figure 11. Radial Temperature Profiles for the Wet Base Case (W1) at t = 1000 Sec. Vertical positions are indicated in the legend, and are the same as in Figure 6.

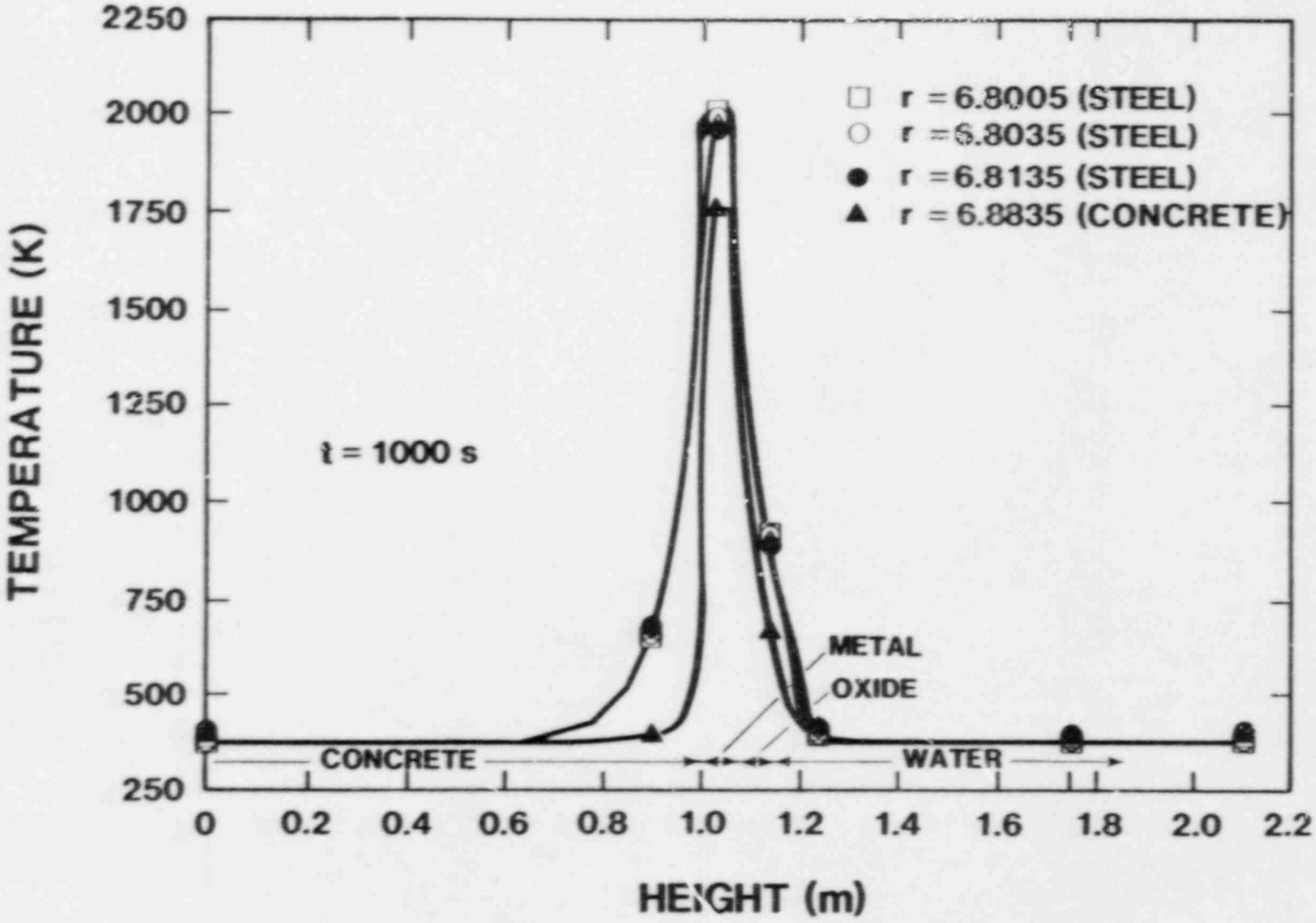

Figure 12. Vertical Temperature Profiles for Case W1, as in Figure 7

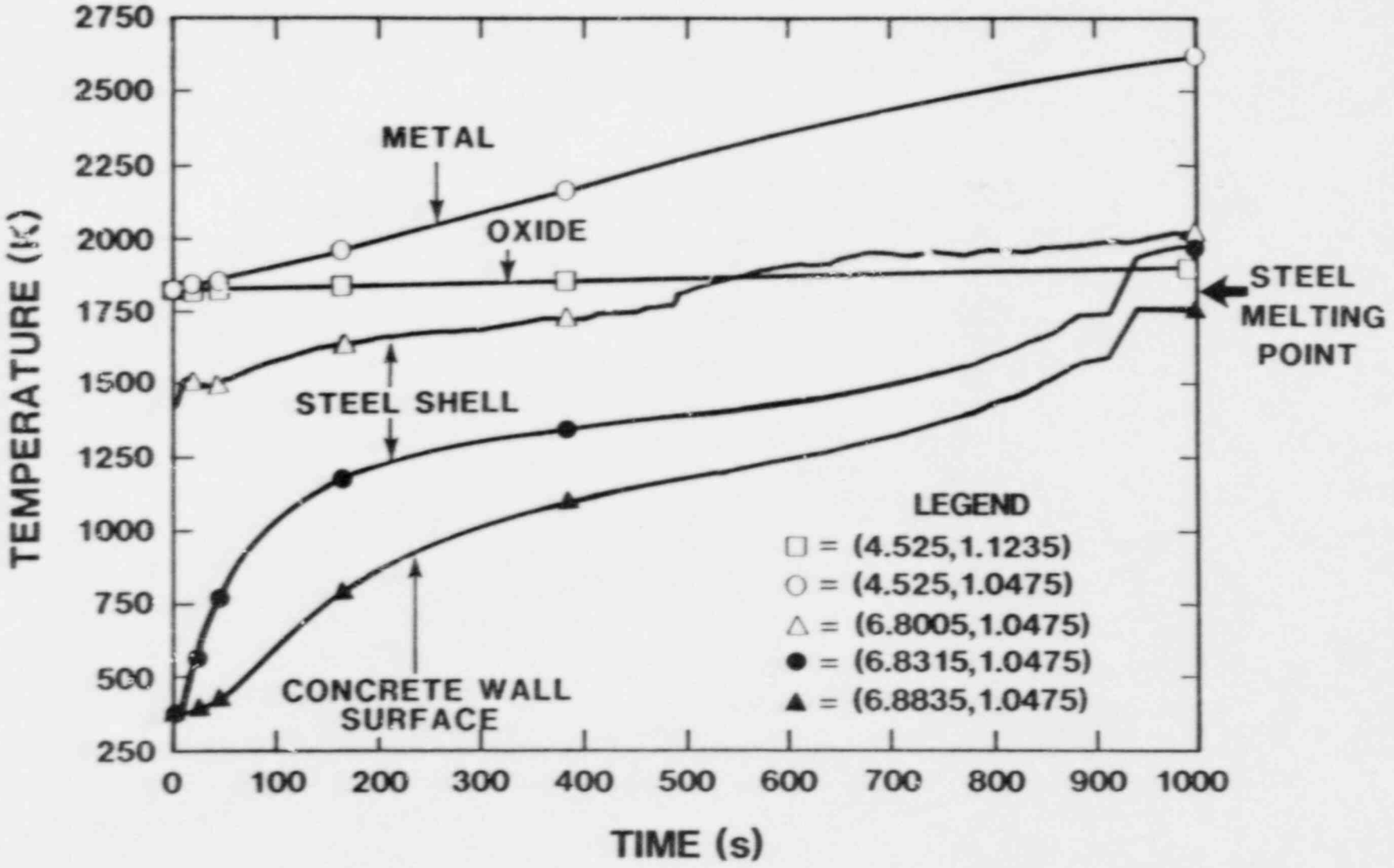

Figure 13. Temperature Histories for the Wet Base Case (W1). Symbols are as in Figure 8.

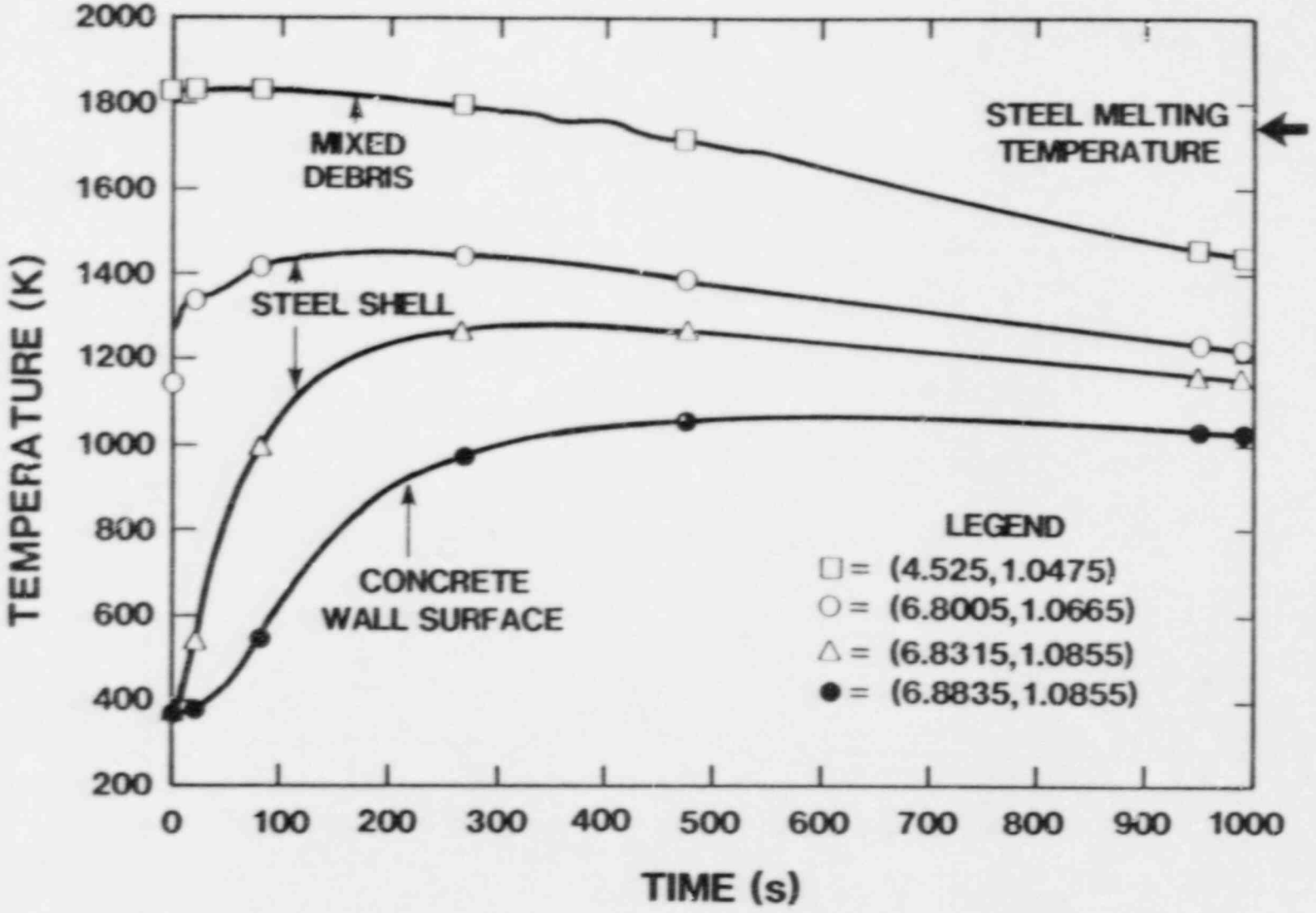

Figure 14. Temperature Histories for Case W3, Which Differ From the Wet Base in That the Mixed Debris Configurations Is Assumed, and the Boiling Heat Transfer Coefficient Is Increased by a Factor of 6. As a result, net cooling of the bulk corium (□) occurs from the beginning of the problem, and the shell does not reach the melting temperature.

heating it as in the previous cases. The corium temperature soon drops below the steel melting point, and no shell ablation occurs. The shell inner surface reaches a peak temperature of 1450 K, and its outer surfaces reaches a peak somewhat later of 1270 K. Though melt-through is not predicted in this case, these very high temperatures suggest that the steel shell will not have adequate strength to survive, because of the dramatic loss of strength of steel at temperatures exceeding 1100 K. This issue is discussed in more detail in Section 4.

3.3 Highlights of Sensitivity Variations

Table 3 presents quantitative highlights of all 23 calculations. These include the dry base case with 10 variations, and the wet base case with 11 variations. In almost all cases, the variation consisted of changing one and only one parameter or feature listed in Table 2 from the base case value. In a few cases, more than one parameter or option was changed at the same time, because of some special interest in the combined variation.

For each case, four temperatures are reported in Table 3. Each is the temperature of the hottest node in the designated region, and each is taken at either the time of shell melt-through or at the time that the back side shell temperature reaches a maximum, in the cases that melt-through does not occur. Also given is the time required for melt-through to be complete for those cases where melt-through occurred. The next two columns are the axial heat losses in MW for the debris, at representative times, in the upward (through the top surface of the debris) and the downward (through the bottom surface) directions. The next column is the residual heat, which is equal to the volumetric heating rate less the two axial loss terms. Since the radial heat loss to the outer radial boundary is small compared to any of these three quantities (at most, 1 MW), the residual power determines the rate at which the debris is heating (positive values) or cooling (negative values). These three quantities can be useful in understanding how the parameter variations affect the overall behavior of the system. The heat fluxes are not output at every timestep. The last column in Table 3 gives the time at which the heat losses were evaluated, which does not precisely coincide with the time of melt-through, but which is generally close enough that the trends seen are representative of conditions at the time of melt-through.

The chemical heat generation models used in these calculations are relatively simplistic and are not time-dependent. Volumetric heat generation from the zirconium oxidation reaction is simply treated as the product of the decay heat generation and the chemical heat generation multiplier (Q*) described in Section 3.1. The chemical heat generation term was held constant until the calculation was terminated. Termination of the calculations occurred for one of two reasons: 1) complete shell melt-through occurred, or 2) a clear indication of failure to melt was achieved. The zirconium oxidation reaction

$$Zr + 2H_2O \longrightarrow ZrO_2 + 2H_2 \qquad (12)$$

liberates 6.82 joules per kilogram of zirconium reacted. Based on the mass fractions of the various debris components present on the drywell floor, we

Table 3. SENSITIVITY STUDY RESULTS

Case	Variations From The Base Case	Temperatures (K)				Time to Peak or Melt	Debris Heat Flow (MW)			Time of Heat Flux Snapshot
		Debris Metal	Debris Oxide	Shell Front	Shell Back		Upward Loss	Downward Loss	Residual	
D-1	Dry Base Case	2610	1900	melt	melt	15.3	3.8	13.0	19.2	17
D-2	$K^* = 2.0$	2932	1951	melt	melt	26.3	3.8	12.6	19.6	17
D-3	D.C. = MIX	2062		melt	melt	66.7†	29.1	3.2	3.7	67
D-4	$Q^* = 2.0$	2232	1982	melt	melt	55.0	3.1	3.5	6.4	67
D-5	$\epsilon_c = 0.30$	2610	1900	melt	melt	14.9	3.8	13.0	19.2	17
D-6	$T_D^o = 2000$ K	2585	2055	melt	melt	12.0	4.7	14.6	16.7	17
D-7	GAP = COND	2458	1880	melt	melt	13.2	3.8	13.1	19.1	17
D-8	L = 0.38 m	2691	1879	melt	melt	11.0	3.9	17.6	49.5	17
D-9	$K^* = 2.0$ D.C. = MIX	2603		melt	melt	75.8†	22.0	3.9	10.1	67
D-10	$T_D^o = 2000$ K GAP = COND L = 0.38 m	2582	2037	melt	melt	8.3	4.9	11.1	55.0	17
D-11	$h_c = 2000$ W/m²K	2580	1900	melt	melt	15.5	3.8	14.8	17.4	17
W-1	Wet Base Case	2610	1891	melt	melt	15.4	7.2	13.0	15.8	17
W-2	$K^* = 2.0$	2932	1956	melt	melt	26.7	6.2	7.3	22.5	28
W-3	D.C. = MIX $h^* = 6.0$	2050		1450	1270	6.0	54.7	1.8	-21.0	17
W-4	$Q^* = 2.0$	2323	1866	melt	melt	63.3	5.2	3.8	4.5	61
W-5	$\epsilon_c = 0.30$	2610	1891	melt	melt	15.0	7.2	13.0	15.8	17
W-6	$T_D^o = 2000$ K	2585	2051	melt	melt	12.2	8.8	14.6	12.6	17
W-7	GAP = COND	2458	1876	melt	melt	13.3	7.3	13.1	15.6	17
W-8	L = 0.38 m	2691	1879	melt	melt	11.2	7.2	17.5	46.3	17
W-9	$Q^* = 2.0$ $\epsilon_c = 0.30$	2323	1866	melt	melt	64.2	5.2	3.8	4.4	61
W-10	$K^* = 2.0$ D.C. = MIX $Q^* = 2.0$ $h^* = 6.0$	1810		1280	1150	10.0	25.1	3.3	-15.9	17
W-11	$h_c = 2000$ W/m²K	2580	1891	melt	melt	15.6	7.2	14.8	14.0	17
W-12	$h^* = 6.0$	2610	1880	melt	melt	15.3	8.6	13.0	14.4	17

†Exceeds nominal zirconium burnout time; see text

can calculate the total quantity of energy that can be liberated from this reaction for a given initial inventory. A more useful quantity is the time required to completely consume the zirconium metal; for the parameters used in this study we find

$$t_{burnout} = 273.0/Q^{*} \text{ (minutes)} \quad . \tag{13}$$

For example, the chemical heat generation multipliers used in this analysis (Q* = 2.0 and Q* = 7.0) correspond to zirconium burnout times of 136.5 min and 39.0 min respectively.

The times required to melt through the shell in two of the calculations listed in Table 3 (cases D3 and D9) exceed the burnout times for their corresponding chemical heat generation rates. Although the norminal burnout time was exceeded in two calculations, we should not necessarily conclude that nonmelting of the shell is implied; in reality, the heat generation rate would change as a function of time, which could significantly influence the melt progression for the same total chemical inventory. Obviously, treating chemical heat generation as constant for all time is an oversimplification of the phenomena (especially when the mass fraction of zirconium in the debris has been significantly depleted). However, a more accurate treatment of the chemical heat generation term would require that a much more mechanistic model be implemented in TAC2D. Implementation of a more mechanistic model was well outside the scope of these calculations. Thus the cases D3 and D9 must be characterized as marginal and inconclusive.

Out of the 21 remaining cases reported, the steel shell was melted through in 19 cases. One of the cases in which the shell did not melt was W3, already discussed in Section 3.2. The other non-melting case was W10, which was a case in which all the sensitivity parameters were set at the one choice out of the two used in other sensitivity variations which was judged to minimize the shell attack.* In contrast to this "all-optimistic" case, the D10 case was "all-pessimistic" in the sense that of the two choices for each parameter or option, the one judged most likely to maximize the liner attack was chosen. As seen in the table, the shell melt-through was most rapid in this case (8 minutes).

The reader should note the careful wording of the above characterization of W10 and D10; in particular, we are not characterizing them as "best-case" or "worst case," since we do not attribute any of the parameter choices to limits on the ranges of the parameters. Two values were associated with each parameter, but these values are not believed to span the uncertainty range; they were chosen as representative values in order to evaluate the variation in output results with a change in input parameters. The cases W10 and D10 were adjuncts to the main one-at-a-time sensitivity study to see how greatly the variations "stacked up" when choices were intentionally made to emphasize or de-emphasize the shell attack.

Both of the cases that did not melt through resulted in very high peak liner temperatures. W3 gave 1450 K and 1270 K for the shell front and back

* All except h_c, which was a sensitivity variable added late in the study.

side temperatures, respectively, while W10 gave 1280 K and 1150 K. In assessing the significance of these results, one should consider the dramatic loss of strength of steels at high temperatures. Figure 15, taken from Reference 17 shows how carbon steels have lost about 90 percent of their tensile strength at temperatures which exceed the transition temperature for conversion from the ferrite/pearlite form to the austenite form of the steel. Peak temperatures of 1200 K will likely cause shell failure in all of the cases studied. Given this failure criteria, failure times would range from 100 to 200 seconds.

The heat loss information shows how the parameter changes affect the various flows of heat from the debris. A particularly clear trend is that in all the layered cases, the dominant heat loss is from the debris is downward, while for the mixed cases, the heat loss is primarily upward. These trends are a result of the insulating nature of the oxide layer, and the high chemical heat generation assumed in the metal layer. It is also relevant to note that the flow of heat from the debris to the liner is always a very small contributor to the total heat loss from the debris. The bulk debris temperature is thus essentially determined by the balance between heat generation and upward and downward losses. This bulk temperature then determines whether the shell will be ablated. Conditions in the gap region are primarily influential in determining the size of the conduction boundary layer (see Figures 7 and 12) and the rate the shell ablates once melting begins. No cases were found in which melting commenced, but was arrested before melt-through occurred.

It is probably inevitable in a straight sensitivity study such as this that some parameter combinations are inconsistent with the predicted results. An example is W2, in which the assumed low thermal conductivity of the metal layer results in the extremely high peak temperature of 2932 K, which is near the boiling point of iron, and which is well above temperatures which CORCON usually predicts. Obviously the low thermal conductivity assumption is inconsistent with this high temperature, but the case is included in the study for completeness. Similarly, the assumption of the mixed configuration and the high enhancement of boiling heat transfer used in case W-10 is somewhat inconsistent with the low chemical heating rate implied by the choice $Q^* = 2.0$, since the former two assumptions are presumably predicted on a vigorous sparging due to an intense ablation process.

4.0 DISCUSSION OF UNCERTAINTIES

4.1 Purpose of Discussion

The ranges of parameters used in the sensitivity study described in Section 3 were somewhat arbitrary, since the intent was strictly to understand the variation of key output quantities as input parameters were varied. The reader is cautioned that there is little relationship between the ranges which appear in Tables 2 and 3 and the current state of phenomenological uncertainty for each parameter. In this section, we will present a limited discussion of the uncertainty ranges. Our intent is principally to identify the numerous sub-issues which come into play in the uncertainty assessment, and only secondarily to express opinions about the numerical ranges.

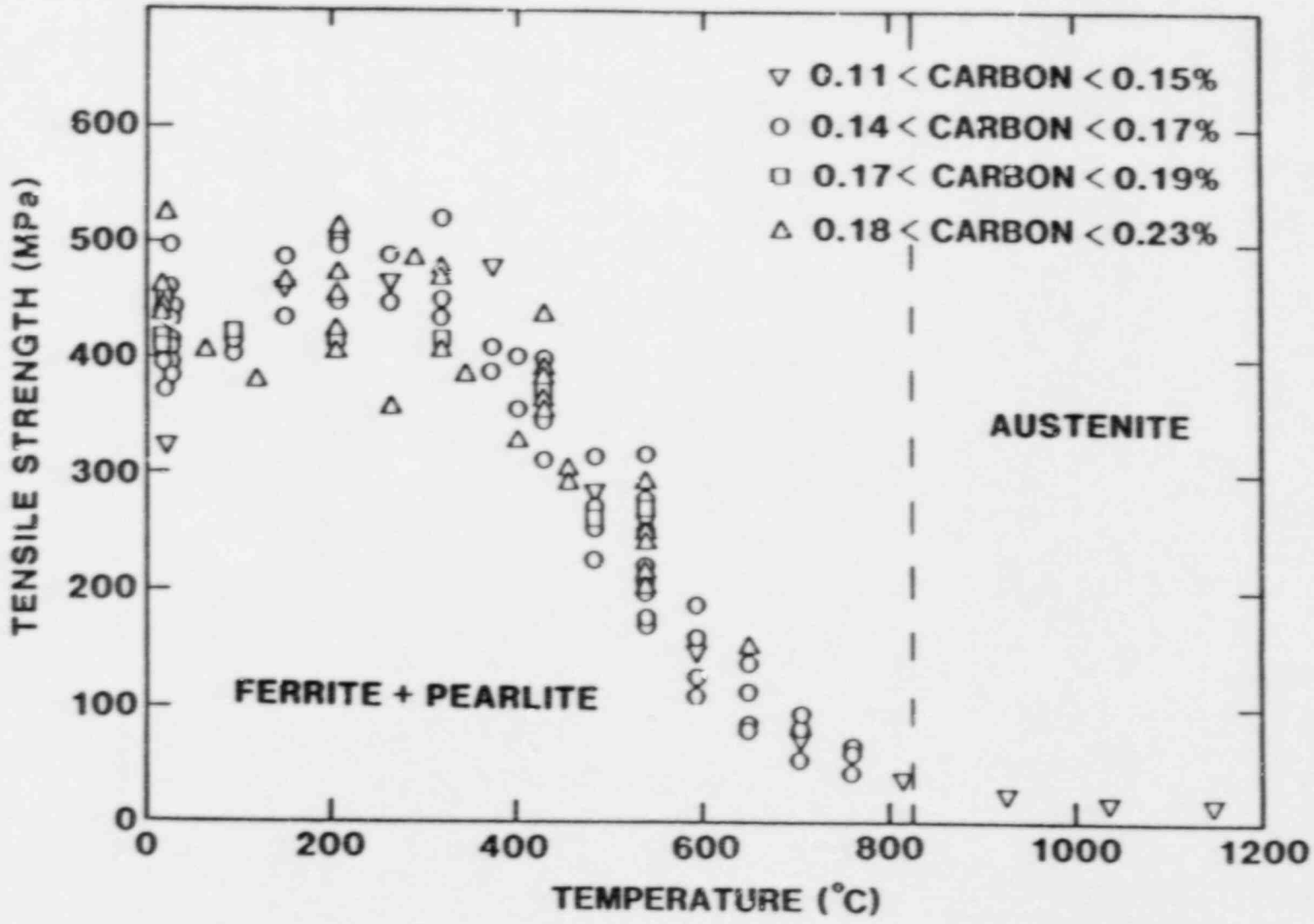

Figure 15. Ultimate Tensile Strength as a Function of Temperature for Carbon Steels With Various Carbon Contents (Reference 15).

The issue of parameter uncertainty ranges is made extremely difficult by the "surrogate parameter" problem. A complete assessment of uncertainties in a calculation must take account of the phenomena that are misrepresented or unrepresented in the model. One way to do this is to treat a phenomenon which is included in the model as a surrogate for another phenomenon which is not. This approach, while it is often unsatisfying and/or impossible, has the advantage of a more complete quantitative assessment of uncertainty than methods that neglect model deficiencies.

For example, debris crust formation is not allowed in the shell contact region in this model. However, the effect of crust formation has been evaluated by performing parametric variations of the debris conductivity. Since the thermophysical effect of crusting limits the effective thermal conductivity, the surrogate approach addresses the impact of crusting. In the current context, the surrogate parameter approach is useful because the pure heat transfer/conduction treatment intrinsically neglects many of the key phenomena. Our discussions of the uncertainty ranges will therefore include references to the uncertainties in the nominal quantities represented by the parameters (e.g., the actual value of the thermal conductivity of the corium) and also to uncertainties which can be captured by treating these parameters as surrogates for processes not modeled (e.g., natural convection heat transfer represented by a broad range of enhanced corium thermal conductivities).

We do not presume, however, to capture all uncertainties with this method. In fact, we will not present overall uncertainty estimates. The limited goal of this part of the study was to provide useful information to members of the expert panels; it is they who must perform the integration process which includes the uncertainties discussed here as well as any uncertainties which are not discussed.

4.2 Uncertainties in Parameters Varied in the Sensitivity Study

4.2.1 Volumetric Heat Generation

The amount of decay heat in the corium pool is relatively well understood, for a given fraction of corium ejected at a given time, but that is probably not the major source of heating. Calculations with debris concrete interaction codes like CORCON indicate that exothermic chemical reactions, particularly oxidation of zirconium, will dominate. The reaction rate is affected not only by the concentration of zirconium in the melt, but also by the rate and composition of gas evolution from the ablating concrete. Peach Bottom has a limestone-aggregate concrete and tends to produce large quantities of steam and carbon dioxide, resulting in a relatively vigorous chemical reaction when zirconium is present. The ratio of chemical energy generation to decay power can exceed 10, and can also be significantly time-dependent. Since the decay power itself is uncertain because of the uncertainty in timing and radioisotopic composition of the debris, this uncertainty becomes a multiplicative factor in the overall uncertainty. The value of 90 W/Kg used for the decay power is based on the ORNL study [6], and should be considered rather low. The melt progression in that study was very slow and earlier corium releases could lead to significantly higher decay power (as high as 200 W/Kg).

4.2.2 Surface Contact Area and Debris Depth

Since the mass of core material ejected affects the corium depth, the in-vessel melt progression will have a large influence on this parameter. Since the corium ejection process is time-dependent, and this analysis assumes a constant mass in the pool, the definition of "mass ejected" requires some interpretation on the part of the analyst attempting to quantify uncertainty. However, given the current state of understanding of BWR in-vessel melt-progression, it is clear that the nominal range of uncertainty for this parameter is large--probably from a few percent to nearly all the core and a large fraction of the steel internals. For a given mass of debris ejected, other phenomena affect the depth of the debris layer. One is the amount of level swell. A 40 percent porosity was assumed in all the calculations, but the actual value could be either greater or smaller. The 0.19 m depth used for most of the calculations was based on a 40 percent porosity, 50 percent of the core material ejected from the vessel, and uniform spreading.

It should be noted that the debris depth and surface contact area will be sensitive to the uniformity of spreading. Under the freeze-thaw conditions likely to be present in the actual spreading process, it is likely that azimuthal spreading in the ex-pedestal region would be inhibited by structures and by the formation of blockages. This could lead to a corium depth larger than the value based on uniform spreading.

4.2.3 Corium Thermal Conductivity

There are important uncertainties in this quantity due to uncertainty in our knowledge of the composition of the debris, and also due to uncertainty in the physical properties of mixtures and eutectics even if the composition is known. However, the principal purpose of the sensitivity study with respect to thermal conductivity was to attempt to capture the effect of convection-dominated heat transfer in the liquid portion of the debris pool. A practical way to simulate convection heat transfer in a conduction code is to enhance the thermal conductivity, which was the method chosen for this analysis. The enhancement needed can be several orders of magnitude. If that were the only issue, a range for this surrogate parameter uncertainty could probably be readily given based on standard correlations for convection heat transfer. However, our treatment of the debris pool does not account for the formation of a solid crust in the contact region. Thus the enhancement in thermal conductivity should not be very excessive, since in the crust region, there is no convection enhancement, and the only uncertainty is the nominal uncertainty. The range of this parameter should therefore be some weighting of the convection-enhanced value for the liquid region, and the nominal value for the solid crust region. We expect the uncertainty range to be larger than is reflected in the sensitivity study but leave the quantitative assessment of this thorny question to others. More sophisticated treatments of crust formation are underway, but definitive results were not available at the time of publication [18].

4.2.4 Gas Emissivity

Absorption and reflection of radiant heat from the gas overlying the debris pool is dominated by the presence of very dense aerosols (the effect of optically active gases is small because the steam and carbon dioxide con-

centrations are calculated to be low during this early phase of the accident [6]). Radiant energy transport in an absorbing/scattering gas is a very difficult calculational problem which is not, moreover, well suited to the lumped treatment of the gas employed in these calculations. Consequently, a small calculational study was commissioned in which a detailed 1D radiation transport model was used to estimate the effective emissivity of the gas/aerosol mixture as used in the TAC2D calculations. Appendix A describes the auxiliary calculations and results. The aerosol conditions assumed corresponded to a CONTAIN code calculation [6] in which CORCON and VANESA were active, resulting in a mass loading in the Peach Bottom cavity of 0.016 kg/m3, and a mean size of 2 microns. The resulting range of effective emissivities was about 0.4 to 0.8. The uncertainty range when other uncertainties besides those considered in the side study are factored in is likely to be somewhat higher. However, the TAC2D sensitivity study indicates that gas emissivity is not likely to be a dominant source of uncertainty for this problem. Note that the gas in the shell-concrete gap was assumed to be transparent and aerosol-free.

4.2.5 Pool Boiling Heat Transfer Coefficient

The normal flat plate pool boiling curve may not be adequate for the conditions at the interface between the debris and the water pool, since gas generation from below could lead to entrainment and tend to break up the interface film. Under these conditions heat transfer between the debris and the overlying water pool would be enhanced. However, it is also possible that at very high superficial gas velocities the gas transmission through a porous crust would increase the film thickness and therefore decrease the heat transfer coefficient.

4.2.6 Debris Configuration (Layered or Mixed)

This uncertainty is not represented as a parameter, but as two alternative choices for the locations of the debris constituents. As discussed in 4.2.3, our treatment of the layered configuration is probably more realistic than our treatment of the mixed configuration. However, it is uncertain which configuration is more representative of what might actually occur. There may be other plausible configurations as well, such as the three-layer arrangement assumed at the start of CORCON calculations, or configurations which are intermediate between the cases considered. A high degree of gas generation would be associated with the mixed configuration, since strong mixing forces would exist. However, this issue is currently controversial and unresolved in the Molten Core Concrete Interaction community. Another configuration would be a pure metal layer with no oxide present, as predicted by some ORNL BWRSAR calculations [6].

4.2.7 Shell-Concrete Gap Heat Transfer

Actual conditions in the gap are somewhat uncertain. As-built drawings indicate that the gap is air, but there is some uncertainty whether the ethafoam insulation was fully removed or has been partially degraded. If removal occurred, some residue (possibly burned) may remain, and it may be non-uniform. If there is an air gap, the model used in TAC2D is sensitive to the steel and concrete emissivities. Although the steel emissivity was not varied (a handbook value of 0.64 was used), the steel may in fact be

well-oxidized, which would tend to increase this value. The concrete emissivity is a good surrogate for uncertainty in the steel emissivity.

The nominal uncertainty range of concrete emissivity at the calculated shell temperatures is rather high, since the temperature dependence is significant, and the data base is scant. Figure 5-20 in Reference 16 suggests a range from 0.35 to 0.5 for the nominal concrete emissivity at the temperatures of interest. Dehydration of the concrete during the heat-up prior to vessel failure would probably lower the emissivity from nominal values. Thus a range of 0.2 to 0.7 may be reasonable.

A few cases were run with a specified heat transfer coefficient between the shell and the concrete wall. These cases represent the possibility that there are regions in which the ethafoam insulation was not removed. The heat transfer coefficient used is based on an assumed insulation thermal conductivity of 0.024 W/m·K. The actual situation may involve partially removed insulation, with a layer of insulating material adjacent to the air gap. The results of such a situation would presumably lie somewhere between the air-gap cases and the fully insulated cases.

4.2.8 Initial Debris Temperature

A value of 1825 K was used for the base case. This was intentionally selected as a rather low value, so as not to make the analysis highly dependent on shell attack during a cool-down of a very hot pool. The value selected was roughly based on early ORNL CONTAIN calculations [6] in which a crude treatment of corium spreading by alternating melting and freezing was the rate-limiting mechanism (the melt release from the vessel occurred over an extended period of time). This approach ensures a debris temperature at or near the solidus at the time the debris contacts the shell. Other spreading or melt ejection scenarios could give significantly higher initial corium temperatures. In particular, in-vessel melt scenarios which lead to a large and rapid release of molten corium would likely result in higher initial temperatures at the time of contact with the steel shell.

4.2.9 Debris-Concrete Heat Transfer

The range of heat transfer coefficients used by CORCON at this interface is quite broad: numbers from 300 to 1000 are s[illegible]n in the CORCON-MOD2 sample problem [3], for example, while some of the cases used for the ORNL study [6] exceeded 2×10^3.

4.3 Uncertainties in Parameters Not Varied in the Sensitivity Study

Only a brief review of the parameters not varied in the TAC2D runs will be given here, since it is more difficult to translate the sensitivity study into an understanding of these uncertainties. The main purpose of this discussion is to remind the reader that not all input parameters to the TAC2D runs were varied in the sensitivity study.

4.3.1 Debris Pool Swell

For the purpose of calculating debris depth, a 40 percent corium pool porosity was assumed. This assumption effectively changes the density of the corium in order to account for the presence of gas bubbles due to the

debris-concrete interactions. The value chosen corresponds to experience with CORCON and experiments, but there is doubtless a good deal of uncertainty associated with this parameter.

4.3.2 Drywell Geometry

There are two important assumptions used in the TAC2D analyses: first, the angle between the shell and the concrete was taken to be 90° (the actual angle is about 45°), and second, a fixed gap between the shell and the concrete was assumed. The former simplification was made because early TAC2D studies showed that the effect of the angle was not dramatic, and the revised geometry was much easier to deal with computationally. The assumption about the presence of the gap was based on a review of the structural studies which have been performed for the pre-vessel failure expansion phase [5], and also a study of drawings which indicated that distortion of the shell to conform both to the floor and to the concrete wall would imply failure in and of itself.

4.3.3 Thermal Properties

Besides the corium and steel thermal conductivity uncertainty discussed in Section 4.2.3, there is also the issue of the nominal material properties of all the other constituents. The most critical of the material properties are those for steel, but the associated uncertainty is probably small. The concrete thermal conductivity could be uncertain by a factor of two or more (in part because of possible dehydration effects), but the impact of this uncertainty is also expected to minor. An uncertainty which affects the energy balance is the effect of heats of formation for the various eutectics or phase changes in the corium (both the metal and oxide components). The larent heats of formation for the various debris components were included in all of the calculations. However, as noted earlier, crusting, and the reduction in the effective thermal conductivity normally associated with crust formation and solidification was not allowed in the models. The corium is treated consistently as a uniform, single phase conducting medium, and the only recognition of fluid vs. solid behavior is in the presence or absence of a large thermal conductivity enhancement, which is present throughout the problem. The phase change energy of steel shell during melting is properly taken into account.

4.3.4 Radiative Contribution to the Film Boiling Heat Transfer

Equations (5) and (11) do not explicitly include radiative heat transfer across the film, and at extremely high surface temperatures (above 1200 K) neglecting radiation could be important. For the horizontal boiling case, the variation of h* is an adequate surrogate for this effect. For the vertical case, no variation was performed which could be a surrogate. However, inspection of Figure 13 reveals that the steel temperatures are relatively low in the pool region and separate calculations indicate that the enhancement due to radiation will be small (less than 10 percent).

4.4 Additional Modeling Uncertainties

Besides the uncertainties associated with input parameters to the TAC2D code, one must also consider ways in which the model fails to capture important phenomena. To some extent, such deficiencies can be assessed

with the surrogate parameter approach, but there are some cases in which this approach is not very useful.

Probably the most important weakness of the model used is the fact that the entire corium pool is treated as a uniform, conducting medium. Enhanced thermal conductivity cases are an attempt to capture the liquid nature of the pool, while the lower values emphasize the effect of the solid crust. What is really needed is detailed analysis of the coupled fluid motion/solid conduction problem, including ablation processes at the liquid/crust interface. No existing calculational tool exists which is suitable for this analysis. This problem is probably less acute for the metal layer in the layered cases, since the overlying oxide layer is treated as frozen (no conductivity enhancement), and the metal typically has some degree of superheat, so a crust at the shell boundary is not likely to be thick or persistent. For the mixed configuration, the impact of this treatment is more difficult to assess, and one must consider a host of issues relating to the degree of stirring, the degree of homogeneity of the metal/oxide mixture, the solidus temperatures for the wide variety of eutectics that can form, and the nature of the freezing process in an agitated slurry which is represented by the mixed configuration.

As has been indicated earlier, the TAC2D model does not include the effect of concrete ablation. One consequence is that the concrete floor develops temperatures in excess of the ablation temperature over a few centimeters at the surface (see Figure 8 for example). The ablation process would tend to increase the downward heat transfer by exposing cooler concrete. One effect of this limitation is the insensitivity of the TAC2D results to h*; by contrast, experience with CORCON shows a greater sensitivity of debris temperature to the downward heat transfer coefficient. Analyses which couple CORCON results to transient conduction [1], [18] do not have this shortcoming, but on the other hand, they are not as self-contained as the TAC2D analysis. One approach to the ablation issue may be to think of the bulk debris temperatures in Table 3 as the sensitivity parameters and to assess the uncertainty range for bulk temperatures based on a more mechanistic model for debris concrete interactions.

Another important phenomenon not properly treated by the current model is the rapid ablation mechanism described in [16] and [17] when molten, superheated metal flows against a solid steel boundary, causing shear surface velocities of the liquid with respect to the solid. Such a process could occur, for example, in the steady-state pool, in which the shear velocities are caused by convection currents enhanced by gas generation. Another possibility is that the initial contact of the corium against the shell is in the form of a wave of molten material exiting the pedestal door and flowing with some non-negligible velocity against the shell. This scenario is more representative of the conditions of the experiments in [17], and the analysis therein suggests that virtually complete ablation could occur even before the back side of the steel became hot.

5.0 SUMMARY AND CONCLUSIONS

A wide variety of calculations have been performed with a standard heat conduction package in order to elucidate the parametric dependencies of the steel drywell shell thermal attack question. While the parameters chosen were intended to be representative of possible conditions at the time

molten debris would contact the shell, we do not claim that they represent a uniform sampling of the uncertainty ranges in the parameter space. However, we have supplemented the calculational study with brief discussions of the uncertainty in the various parameters and models which have gone into the calculations. The purpose of this discussion was to assist the members of the NUREG-1150 expert panels to translate the results of the sensitivity studies into assessments of phenomenological uncertainty as specified in the Containment Event Tree.

Almost all of the cases considered resulted in shell melt-through, on time scales ranging from 8 to 67 minutes after initial contact. In 2 of the 21 cases the shell heated to a peak temperature above 1100 K, then began to cool. Both of these cases corresponded to mixed debris configurations, for which the deficiencies in the present modeling are somewhat greater than for the layered configuration. In all cases, the liner temperature reached values so high that failure by creep-rupture due to loss of strength must be considered. Peak temperatures near 1200 K will likely cause shell failure in all of the cases studied. Given this failure criteria instead of the melt-through criterion, failure times would range from 100 to 200 seconds. It is noteworthy that the overall pattern of results reported here is qualitatively similar to the results originally presented in Reference 1 by Greene, who used a more sophisticated treatment of the debris concrete interaction (CORCON-Mod1) but a more simplistic treatment of transient conduction effects.

Ultimately, shell melt-through appears to be controlled by the bulk debris temperature: the shell does not begin to ablate until the bulk debris temperature exceeds the sum of the melting point of the shell plus the temperature drop across the conduction boundary layer identified earlier. The bulk debris temperature in turn, tends to be controlled strictly by the balance between the upward and downward (axial) heat losses and the volumetric heat generation. Since the radial heat loss to the shell is relatively small when compared to the axial losses, its principle effect is to establish the temperature drop across the conduction boundary layer. Modeling limitations of the present approach imply relatively high uncertainty about the magnitude of the conduction boundary layer temperature drop. The simultaneous effects of fluid motion, crusting, and slurry formation in the vicinity of the shell/debris interface region are not modeled. However, the sensitivity variations included in this analysis are intended to provide insight into the ultimate effects that the unmodeled phenomena might have on the shell melt-through issue.

In the layered configurations, shell melt-through times, shell temperature histories, metallic debris temperature histories, and even oxidic debris temperature histories showed little or no sensitivity to changing the drywell environment from a gaseous atmosphere to an overlying water pool. The overall lack of sensitivity is attributed to the effectiveness of the oxide debris layer in insulating the underlying metallic debris layer from the conditions present in the drywell atmosphere.

Four of the calculations performed utilized mixed debris configurations. The results of these calculations were significantly different from the results of the layered cases. The two mixed cases that included an overlying water pool clearly did not melt through. Although the other two mixed cases (which utilized an aerosol-filled drywell atmosphere) resulted in

complete shell melt-through, the times required to attain melt-through clearly exceeded the time at which the zirconium would have been exhausted at the chemical heating rates assumed in the analyses.

Results from the mixed debris calculations indicate that the ultimate melt-through of the shell may have a strong dependence on the geometric makeup of the debris. The layered debris calculations in which metallic debris resided beneath oxidic debris generally resulted in shell melting in very short times with the metallic debris promoting virtually all of the shell ablation. No calculations were performed in which the oxidic debris resided beneath the metallic debris, but the results obtained during this analysis indicate that such a configuration might have a more benign impact on shell ablation. The metallic debris layer would be much more closely coupled to the drywell environment and would therefore not be as likely to reach the highly elevated temperatures attained in the layered cases analyzed here.

It has been emphasized that TAC2D is not the ideal calculational tool in all respects for this problem, and that a number of uncertainties exist which were not explored with sensitivity studies. Thus it would be inappropriate to conclude, based on this study, that drywell shell failure is inevitable whenever debris contacts the shell. Clearly, one could imagine, for example, small amounts of corium released resulting in a shallow layer of debris in thermal contact with the shell, such that the shell could reject the heat at a sufficient rate that excessive temperatures are not reached. On the other hand, the study indicates that for more substantial corium pool depths, shell failure is likely within minutes for a broad range of assumptions about other aspects of the problem.

REFERENCES

1 G. A. Greene, K. R. Perkins, and S. A. Hodge, "Mark I Containment Drywell: Impact of Core-Concrete Interactions on Containment Integrity and Failure of the Drywell Liner," Proceedings of the International Symposium on Source Term Evaluation for Accident Conditions, IAEA, October 1985.

2 "Reactor Risk Reference Document," NUREG-1150, Vol. 1, Draft for Comment, February 1987.

3 Attachment to letter from K. D. Bergeron to NUREG-1150 MCCI Panel Members dated 2/18/88

4 J. J. Weingardt and K. D. Bergeron, ANS Winter Meeting, October 1988, Washington, D.C. (to be published).

5 R. K. Cole, D. P. Kelly, and M. A. Ellis, CORCON-MOD2: A Computer Program for Analysis of Molten-Core Concrete Interactions, NUREG/CR-3920, SAND84-1246, Sandia National Laboratories, Albuquerque, NM, 1984.

6 J. F. Petersen, "TAC2D - A General Purpose Two-Dimensional Heat Transfer Computer Code," Gulf General Atomic, San Diego, California, 1969.

7 K. Mokhtarian, "Mark I Containment Severe Accident Analysis," CBI NA-CON, Inc., April 1987.

8 C. R. Hyman, "Multicell CONTAIN Analysis of BWR MK I Drywell Response and Time-Dependent Vessel Release of Core Debris," presented at Severe Fuel Damage Program Review Meeting, Silver Springs, MD, October 19-23, 1987; also S. R. Greene, et al., letter report dated February 1, 1988, distributed at BWR Mark I Workshop, February 24-26, 1988, Baltimore, MD.

9 C. R. Weast and G. L. Tove, CRC Handbook of Chemistry and Physics, 53rd Edition, 1972-73.

10 C. R. Hyman and C. F. Weber, Effects of Lateral Separation of Oxidic and Metallic Core Debris on the BWR MK-I Containment Drywell Floor, NUREG/CR-4610, Oak Ridge National Laboratory, January 1987.

11 B. V. Karlekar and R. M. Desmond, Engineering Heat Transfer, (West Publishing Co., New York, 1977).

12 J. P. Berenson, Transition Boiling Heat Transfer From A Horizontal Surface, MIT Technical Report No. 17, Mechanical Engineering Department, 1960.

13 G. A. Greene, "Gas Bubbling - Enhanced Film Boiling of Freon 11 on Liquid-Metal Pools," Transactions of the American Nuclear Society, 49, pp. 249-251, June 1985.

14 W. H. Rohsenow, "A Method of Correlating Heat Transfer Data for Surface Boiling of Liquids," Transactions of the American Society of Mechanicel Engineers, 74 (3), pp. 969-976, 1952.

15 N. Zuber, M. Tribus, and J. W. Westwater, "The Hydrodynamic Crisis in Pool Boiling of Saturated and Subcooled Liquids," 2nd International Heat Transfer Conference, Paper 27, Denver, CO, 1961.

16 L. A. Bromley, "Heat Transfer in Stable Film Boiling," Chemical Engineering Progress Series, 46, pp. 221-227, 1950.

17 R. Siegel and J. R. Howell, Thermal Radiation Heat Transfer, (2nd ed.), (New York, McGraw Hill, 1981).

18 D. A. Powers and F. E. Arellano, Erosion of Steel Structures by High Temperature Melts, NUREG/CR-2284, SAND81-1755, Sandia National Laboratories, Albuquerque, NM, June 1983.

19 D. A. Powers, Nuclear Science Engineering, 88, pp. 357, 1984.

20 T. S. Kress, Oak Ridge National Laboratories, presentation to the BWR Mark I Workshop, February 24-26, 1988, Baltimore, MD.

APPENDIX A

Radiative Heat Transfer Through Aerosol Cloud

W. A. Gu, Jack Tills and Associates, Inc., Albuquerque, NM

The problem at hand can be described as follows: Aerosol (metal oxide) cloud from core concrete interaction suspended in an atmosphere at a pressure 1 atm and a temperature of 1100 K. The mass loading of aerosol is 0.016 Kg/m^3 with a mass mean diameter of 2 μm. The boundary surfaces have a temperature of 1500 to 2000 K and an emissivity of 0.8. Due to the relatively large aerosol mass loading, the gas may be treated as transparent to thermal radiation.

To evaluate the optical properties of the aerosol using the Mie theory, the refractive indices ($m = n(1-ix)$) and the material densities (ρ_1) of aerosol are needed, and typical values can be found as follows [1]:

	n	ρ_1(Kg/m^3)
$CaCO_3$	: 1.49-1.68	2930.0
MgO	: 1.74	3580.0
MnO	: 2.16	5450.0
Mn_3O_4	: 2.46	4856.0
CaO	: 1.84	2300.0
Fe_2O_3	: 2.94,3.01	5240.0
FeO	: 2.32	5700.0
SiO_2	: 1.49	2260.0

Unfortunately, the imaginary part of the refractive indices (x) for dielectric material like metal oxide is seldom available in the literature, and the real part (n) is reported for visible light at room temperatures. Thus, a sensitivity study on the optical properties of metal oxide particles of interest is first performed.

The aerosol cloud is assumed to follow the lognormal size-distribution, i.e.,

$$m(D)dD = \frac{1}{\sqrt{2\pi}a} \exp\left[\frac{-\ln^2(D/D_m)}{2a^2}\right]\frac{dD}{D} \quad , \tag{1}$$

where D is the diameter, a is the natural logarithm of the standard deviation, and D_m is the mass mean diameter. The extinction, absorption and scattering coefficients of the particle cloud can thus be defined as

$$\sigma_i = \frac{3}{2\rho_t}\int_0^\infty \frac{Q_i(D)m(D)dD}{D} \quad , \tag{2}$$

where ρ_a is the bulk density of aerosol, $Q_i(D)$ is the efficiency factor, and subscripts i = s, a or t for scattering, absorption and extinction, respectively. The scattering phase function $P(\Theta)$ is defined as

$$P(\theta) = \int_0^\infty P(\theta,D) \frac{N(D)dD}{N_{tot}} \quad , \tag{3}$$

where $P(\theta,D)$ is the scattering phase function for particles with diameter D, $N(D)dD$ is the number density for particles with diameter D, and N_{tot} is the total number density of the particles, i.e.,

$$N_{tot} = \int_o^\infty N(D)dD \quad . \tag{4}$$

In the figures are shown the extinction coefficient (Figure A1(a)), the absorption coefficient (Figure A1(b)), and the scattering coefficient (Figure A1(c)), as a function of n for various values of x, and a = 1. It can be seen that the absorption coefficient vanishes at x = 0. Figure A2 shows the coefficients as a function of n for various values of a, and x = 0.2

To compute the radiative heat transfer through the aerosol cloud, a computer code for one-dimensional slab geometry using S_n solution technique was used. With proper boundary conditions, the angular distribution of thermal radiation fluxes, $I(x,\mu)$, can thus be found, where x is the distance from the left wall, and μ is the cosine of the angle between a particular direction and x - axis. The scalar flux and radiative heat flux can then be evaluated via

$$\phi(x) = 2\pi \int_{-1}^{1} I(x,\mu)d\mu \quad , \tag{5}$$

$$q(x) = 2\pi \int_{-1}^{1} I(x,\mu)\mu d\mu \quad . \tag{6}$$

Also, one may compute the effective emittance and absorptance of the aerosol cloud. First, let's define the radiation flux incident on the wall from the particle cloud as

$$q_{wi} = 2\pi \int_0^{-1} I(x=0,\mu)\mu d\mu \quad . \tag{7}$$

Then the effective emittance may be defined as

$$\epsilon_p = \frac{q_{wi}}{\hat{\sigma}T_p^4} \tag{8}$$

where $\hat{\sigma}$ is the Stefan-Boltzmann constant, and T_p is the particle temperature. The effective absorptance can be found to be

$$\alpha_p = \frac{\frac{q(x=0)}{\dot{\sigma}} + \epsilon_p T_p^4}{T_w^4} \quad , \tag{9}$$

where T_w is the wall temperature. The radiative heat flux at wall can thus be expressed as

$$q(x=0) = \dot{\sigma} \left[\alpha_p T_w^4 - \epsilon_p T_p^4 \right] \quad . \tag{10}$$

Alternatively, one may define an effective emissivity $\bar{\epsilon}$ for the transport medium (aerosol cloud), i.e.,

$$q(x=0) = \frac{\dot{\sigma}(T_w^4 - T_p^4)}{\frac{1}{\epsilon_w} + \frac{1}{\bar{\epsilon}} - 1} \quad , \tag{11}$$

where ϵ_w is the wall emissivity.

Table 1 lists the effective emittance ϵ_p, absorptance α_p, effective emissivity $\bar{\epsilon}$, scalar flux $\phi(x = 0)$, and radiative heat flux at wall $q(x = 0)$ for $n = 2.0$, $a = 0.693$, 1.0 and 2.0, and various values of x. It can be seen that the effective emittances are greater than unity due to the fact that part of the thermal radiation emitted by the wall is reflected back to the wall as a result of scattering. Finally, as the albedo of scattering increases, the effective emittance increases while the heat flux at wall decreases accordingly.

Reference: [1] C. W. Robert, Ed., CRC Handbook of Chemistry and Physics, 65th edition, CRC Press, Inc. (1984-1985).

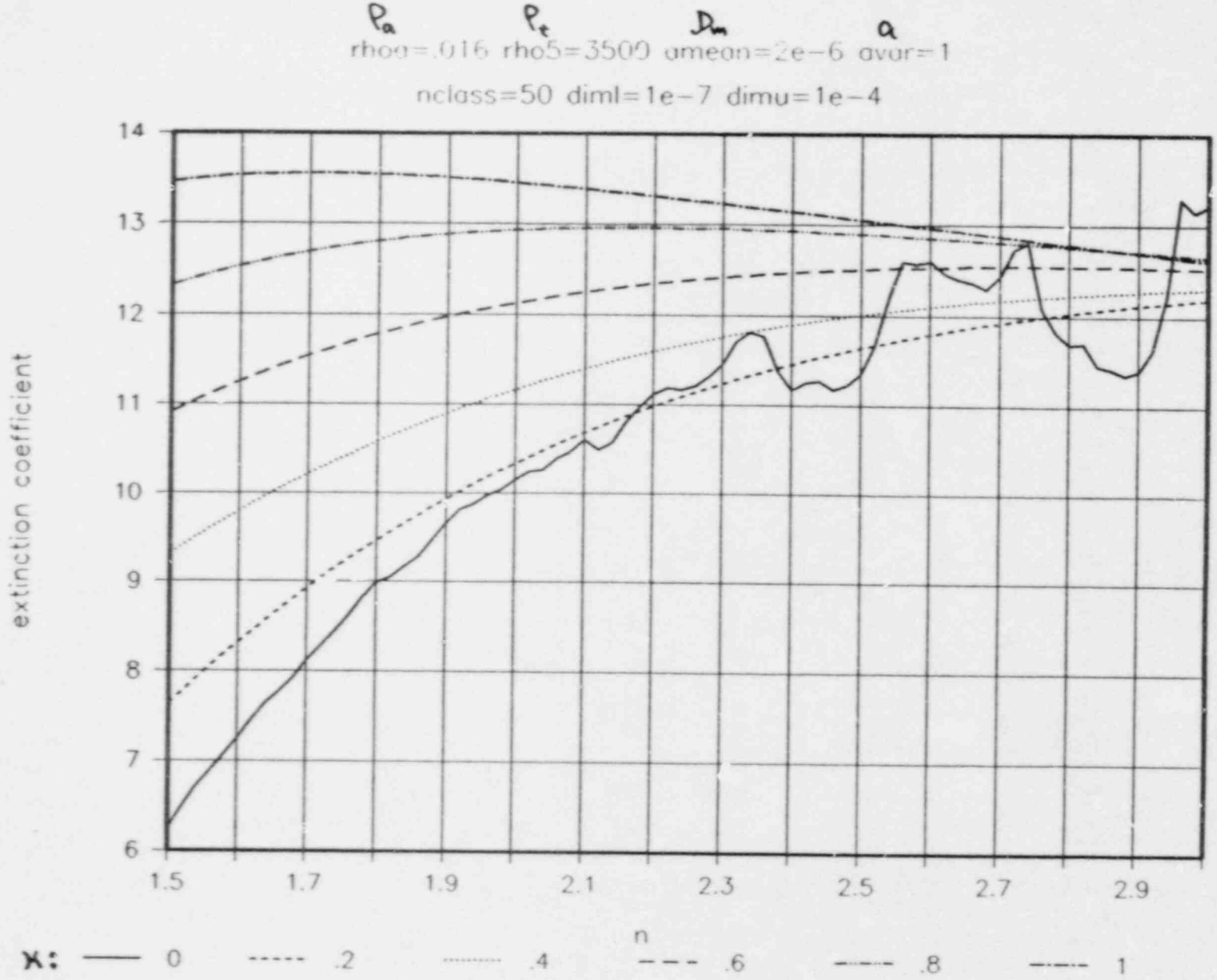
ρ_a ρ_t D_m σ
rhoa=.016 rho5=3509 amean=2e-6 avar=1
nclass=50 diml=1e-7 dimu=1e-4
extinction coefficient
14
13
12
11
10
9
8
7
6
1.5
1.7
1.9
2.1
2.3
2.5
2.7
2.9
n
X: 0 .2 .4 .6 .8 1

Figure A1(a)

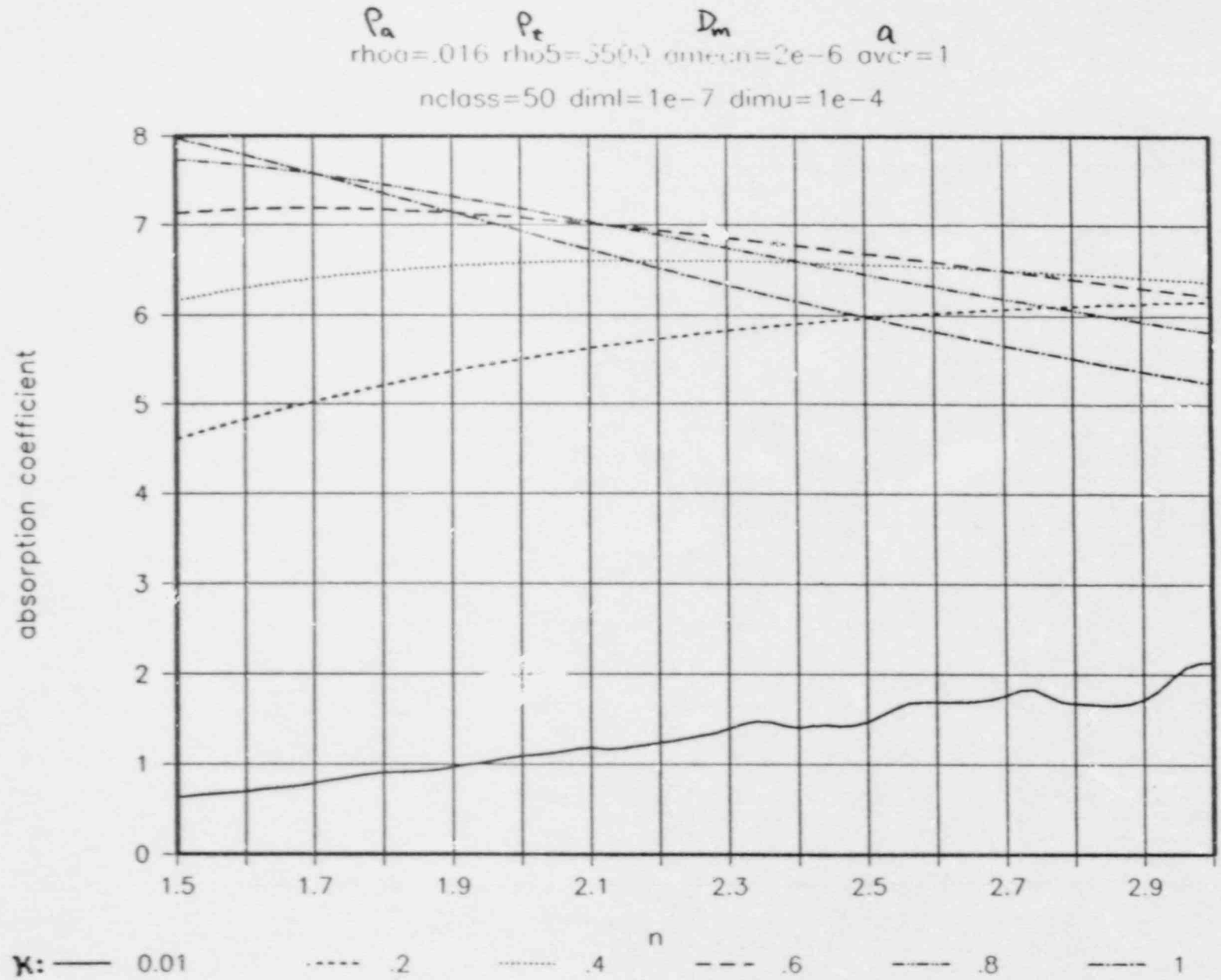
ρ_a ρ_t D_m a
rhoa=.016 rho5=3500 dmean=2e-6 aver=1
nclass=50 diml=1e-7 dimu=1e-4
absorption coefficient
0
1
2
3
4
5
6
7
8
1.5
1.7
1.9
2.1
2.3
2.5
2.7
2.9
n
K: 0.01 .2 .4 .6 .8 1

Figure A1(b)

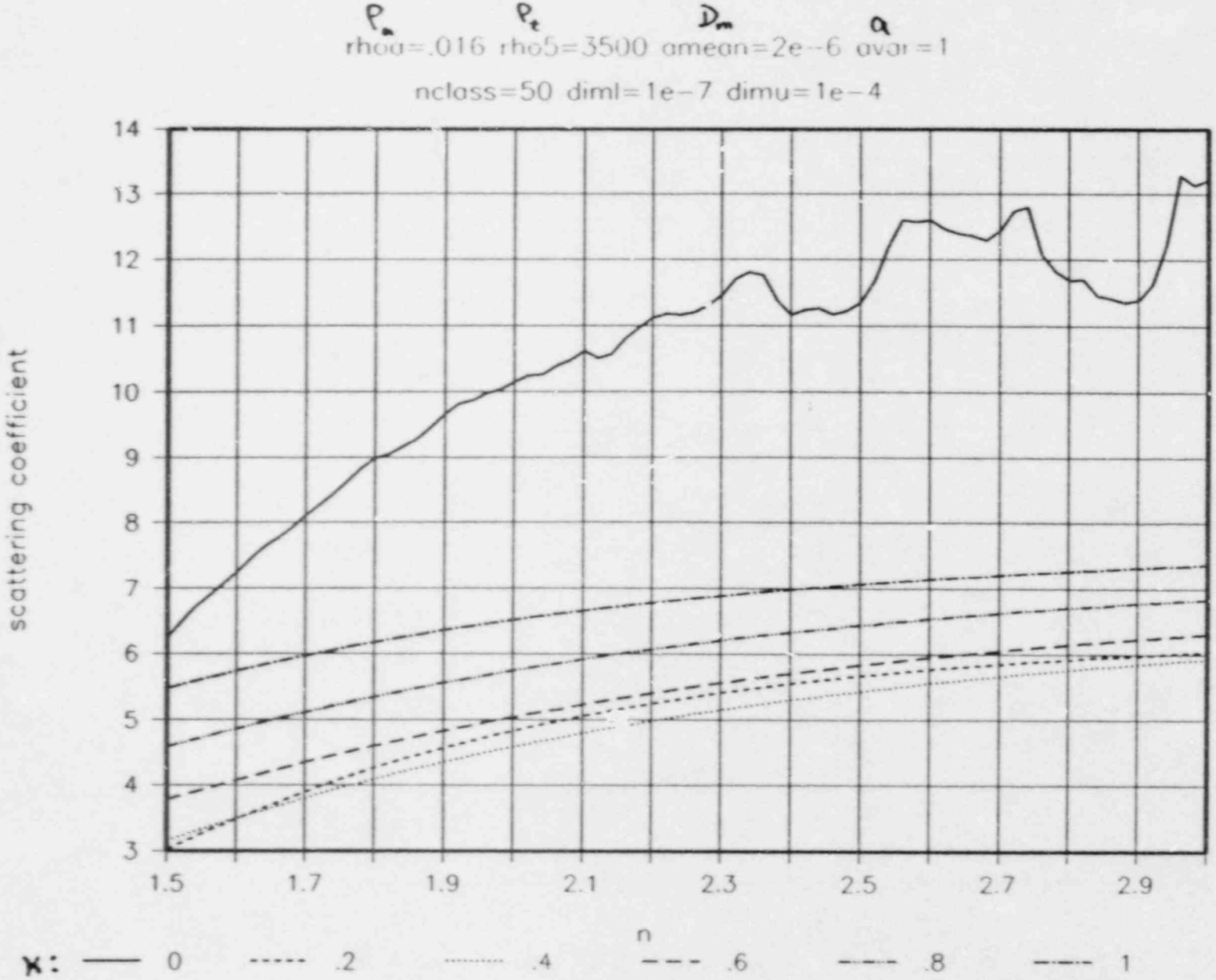
ρ_a ρ_t D_m σ
rhoa=.016 rho5=3500 amean=2e-6 avar=1
nclass=50 diml=1e-7 dimu=1e-4
scattering coefficient
14
13
12
11
10
9
8
7
6
5
4
3
1.5
1.7
1.9
2.1
2.3
2.5
2.7
2.9
n
x: 0 .2 .4 .6 .8 1

Figure A1(c)

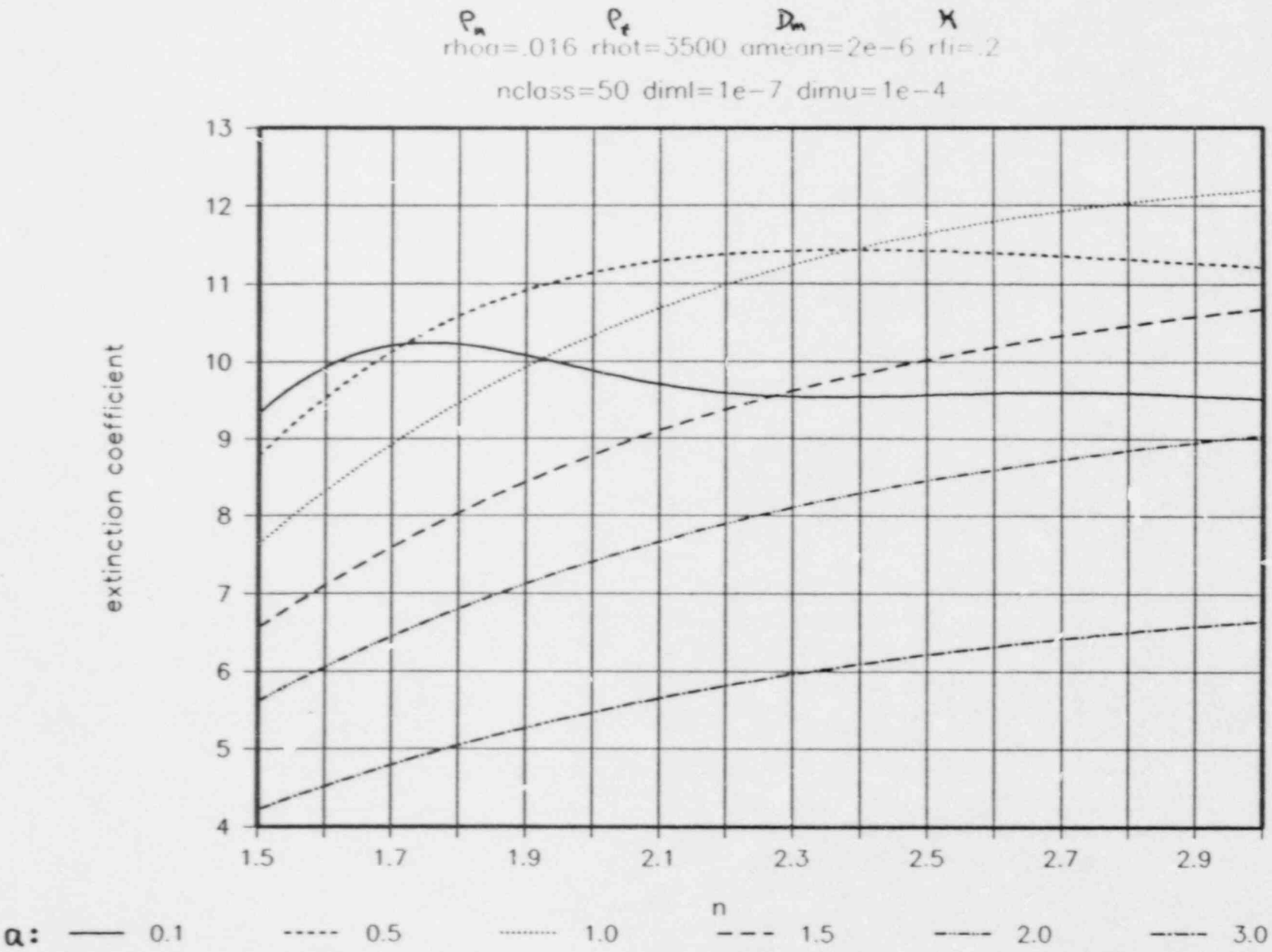
ρ_m ρ_f D_m K
rhoa=.016 rhot=3500 amean=2e-6 rfi=.2
nclass=50 dimi=1e-7 dimu=1e-4
extinction coefficient
13
12
11
10
9
8
7
6
5
4
1.5
1.7
1.9
2.1
2.3
2.5
2.7
2.9
n
a: 0.1 0.5 1.0 1.5 2.0 3.0

Figure A2(a)

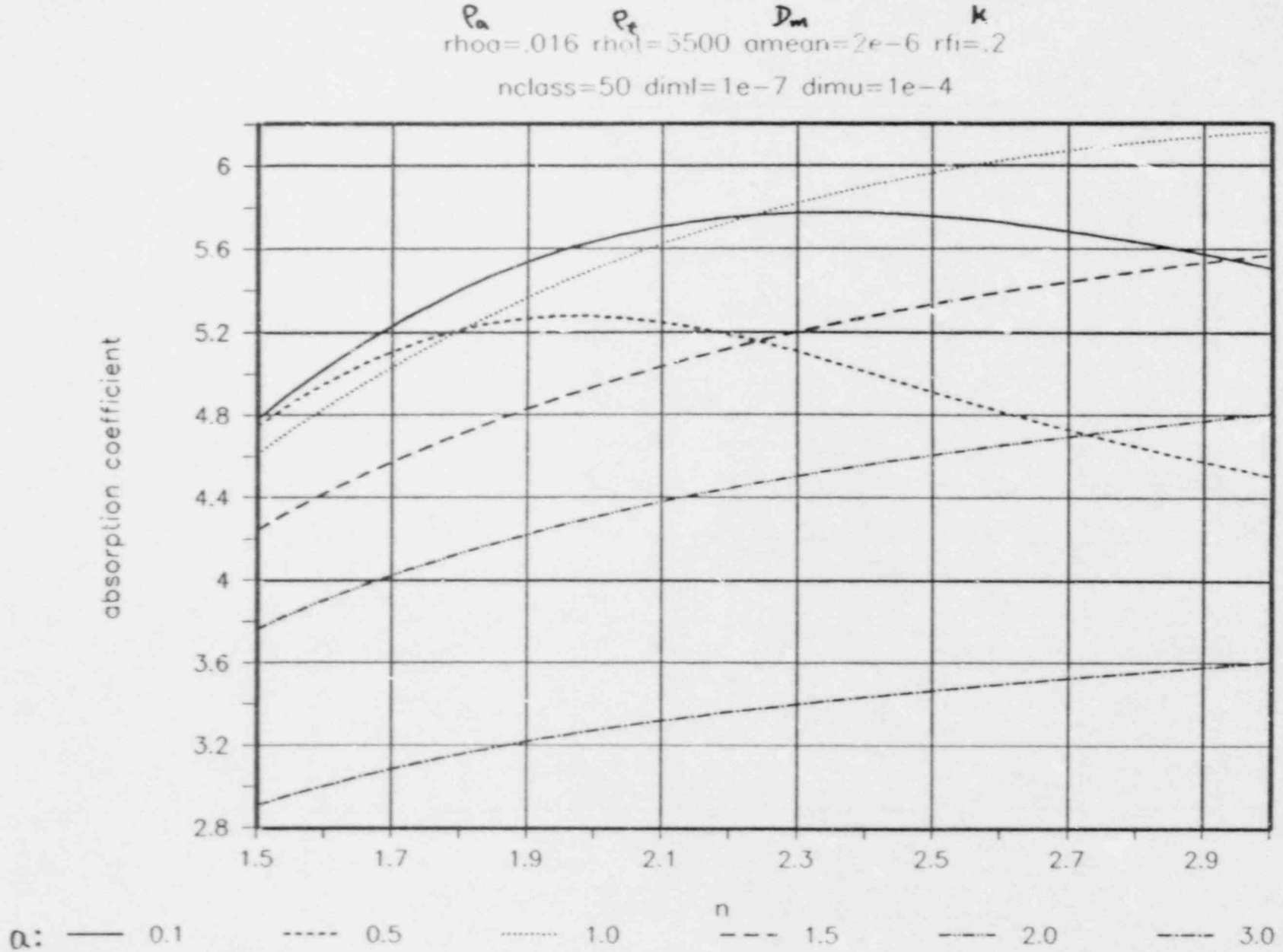
ρ_a ρ_f D_m k
rhoa=.016 rhol=3500 amean=2e-6 rfi=.2
nclass=50 diml=1e-7 dimu=1e-4
absorption coefficient
6
5.6
5.2
4.8
4.4
4
3.6
3.2
2.8
1.5
1.7
1.9
2.1
2.3
2.5
2.7
2.9
n
a: 0.1 0.5 1.0 1.5 2.0 3.0

Figure A2(.)

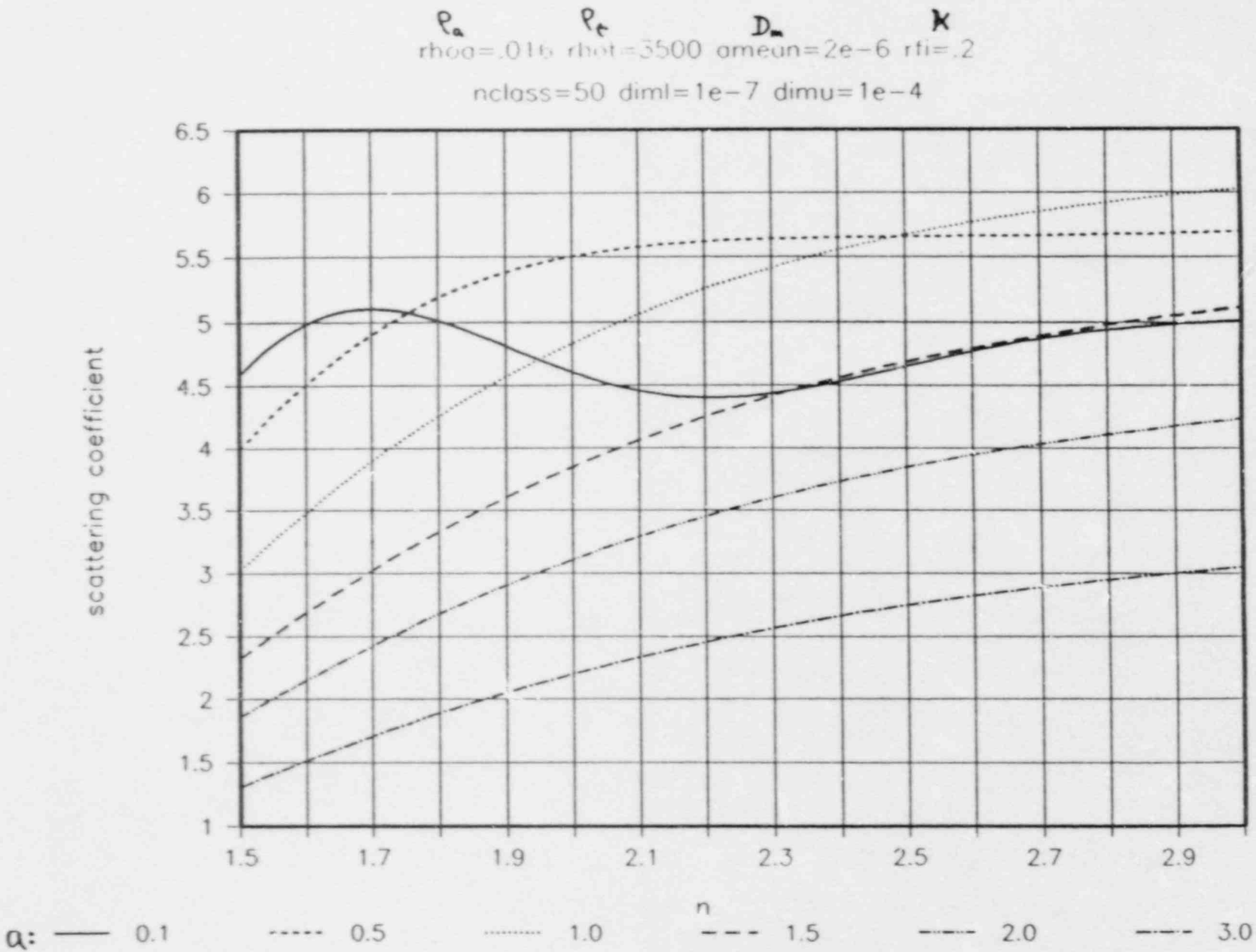
rhoa=.016 rhot=3500 ameun=2e-6 rfi=.2
nclass=50 diml=1e-7 dimu=1e-4
scattering coefficient
6.5
6
5.5
5
4.5
4
3.5
3
2.5
2
1.5
1
1.5
1.7
1.9
2.1
2.3
2.5
2.7
2.9
n
a: 0.1 0.5 1.0 1.5 2.0 3.0

Figure A2(c)

n = 2.0 a = 0.693

*	σ_1	albedo	ϵ_1	a_1	$\bar{\epsilon}$	$\phi(x=0)$	$q(x=0)$
1.0	12.652	0.53466	3.1499	0.89834	0.548	150.53	21.621
0.8	12.269	0.49341	2.9412	0.89199	0.587	146.44	22.974
0.6	11.750	0.46018	2.8269	0.88826	0.610	144.02	23.766
0.4	11.248	0.44626	2.8890	0.89020	0.598	145.23	23.354
0.2	11.089	0.48745	3.7147	0.91598	0.442	161.49	17.871
0.18	11.114	0.49877	3.9703	0.92396	0.396	166.46	16.173
0.16	11.149	0.51259	4.3326	0.93527	0.332	173.44	13.768
0.14	11.196	0.52960	4.8887	0.95263	0.238	184.08	10.075
0.12	11.255	0.55077	5.8737	0.98338	0.08	202.70	3.5344

n = 2.0 a = 1.0

*	σ_1	albedo	ϵ_1	a_1	$\bar{\epsilon}$	$\phi(x=0)$	$q(x=0)$
1.0	13.456	0.48456	1.9515	0.86093	0.789	126.26	29.579
0.8	12.939	0.44454	1.8552	0.85792	0.810	124.18	30.218
0.6	12.132	0.41593	1.7966	0.85609	0.822	122.90	30.608
0.4	11.174	0.41088	1.8093	0.85649	0.820	123.16	30.523
0.2	10.341	0.46774	2.0468	0.86390	0.769	128.19	28.946
0.1	10.118	0.56961	2.6054	0.88134	0.654	139.71	25.237
0.08	10.099	0.60666	2.8952	0.89031	0.597	145.56	23.313
0.06	10.092	0.65506	3.4099	0.90646	0.499	155.76	19.895
0.04	10.096	0.72132	4.7049	0.94689	0.269	180.73	11.295
.035	10.099	0.7420	5.4923	0.97147	0.140	195.60	6.0670

n = 2.0 a = 2.0

*	σ_1	albedo	ϵ_1	a_1	$\bar{\epsilon}$	$\phi(x=0)$	$q(x=0)$
1.0	11.615	0.39477	1.6026	0.85003	0.864	118.77	31.896
0.8	11.142	0.35774	1.5307	0.84779	0.880	117.18	32.373
0.6	10.195	0.33627	1.4934	0.84663	0.888	116.34	32.621
0.4	8.8779	0.34298	1.5137	0.84726	0.884	116.79	32.486
0.2	7.4191	0.41970	1.7031	0.85317	0.843	120.92	31.228
0.1	6.7364	0.53866	2.0988	0.86553	0.758	129.33	28.600
0.08	6.6099	0.57996	2.2841	0.87131	0.720	133.18	27.370
0.06	6.4881	0.63280	2.5811	0.88058	0.659	139.25	25.398
0.04	6.3715	0.70356	3.1601	0.89866	0.546	150.83	21.553
0.02	6.2615	0.80644	5.1692	0.96139	0.192	189.44	8.2123
.018	6.2510	0.81968	5.7543	0.97966	0.099	200.47	4.3271

Table 1. Results of the S_n calculation. $T_0 = 1750K$, $T_1 = 1100K$, $\epsilon_0 = 0.8$.

APPENDIX B

Base-Line Thermophysical Debris Properties

Thermophysical debris properties are defined within the TAC2D code through a series of function subprograms. Except for the uranium oxide, thermophysical properties for each of the individual debris constituents are described by temperature-dependent quadratic data fits (where appropriate) in separate, low-level, function subprograms. Uranium oxide properties were obtained from sophisticated function subprograms (FCON3 and CFUEL) within TAC2D developed by Randall O. Gauntt of Sandia National Laboratories. Higher-level function subprograms are then used to combine the data generated by the low-level subprograms into appropriately weighted average thermophysical properties for each of the general debris categories (mixed, oxidic, or metallic). The data included in the low-level routines are given in Table B1 for the thermal conductivity and Table B2 for the specific heat. (Note: Fe, Cr, and Ni thermophysical properties are represented by carbon steel (CS) properties.)

The weighting factors used in the higher-level subprograms are the volume and mass fractions given earlier in Table 1 for the thermal conductivity and specific heat, respectively. Appropriately weighted thermal conductivities and specific heats for each of the three debris categories discussed in this report are presented in Tables B3 and B4.

Table B1

Thermal Conductivities (W/m·K) as a Function of Temperature (K)

$$K^{*}_{UO_2} = 9.560 - 7.302e\text{-}3\ T + 1.789e\text{-}6\ T^2$$

$$K_{ZrO_2} = 1.658 + 6.834e\text{-}4\ T - 1.371e\text{-}7\ T^2$$

$$K_{FeO} = 20.0$$

$$K_{CS} = 45.8 - 2.25e\text{-}2\ T$$

$$K_{ZIRC} = 14.6 - 4.009e\text{-}3\ T + 1.071e\text{-}4\ T^2$$

*This is a quadratic fit to a sampling of data obtained from FUNCTION FCON3.

Table B2

Specific Heats (J/Kg·K) as a Function of Temperature

$$C_{P_{UO_2}}^{\dagger} = 369.8 - 1.812e\text{-}1\ T + 9.487e\text{-}5\ T^2$$

$$C_{P_{ZrO_2}} = 538.0 + 9.680e\text{-}2\ T$$

$$C_{P_{FeO}} = 500.0$$

$$C_{P_{CS}} = 450.0$$

$$C_{P_{ZIRC}} = 221.4 + 0.224\ T - 7.280e\text{-}5\ T^2 \qquad T < 1090$$

$$= -7.654e4 + 1.326e2\ T - 5.691e\text{-}2\ T^2 \qquad 1090 < T < 1248$$

$$= 356.0 \qquad T > 1248$$

† This is a quadratic fit to a sampling of data obtained from FUNCTION CFUEL.

Table B3

Debris Thermal Conductivitis (W/mK)

MIXED DEBRIS

$$K = 0.416\ K_{UO_2} + 0.213\ K_{ZrO_2} + 0.009\ K_{FeO}$$

$$+ 0.209\ K_{CS} + 0.153\ K_{ZIRC}$$

OXIDIC DEBRIS

$$K = 0.653\ K_{UO_2} + 0.334\ K_{ZrO_2} + 0.014\ K_{FeO}$$

METALLIC DEBRIS

$$K = 0.579\ K_{CS} + 0.421\ K_{ZIRC}$$

Table B4

Debris Specific Heats (J/Kg·K)

MIXED DEBRIS

$$C_p = 0.541\ C_{P_{UO_2}} + 0.141\ C_{P_{ZrO_2}} + 0.005\ C_{P_{KeO}}$$

$$+ 0.195\ C_{P_{CS}} + 0.118\ C_{P_{ZIRC}}$$

OXIDIC DEBRIS

$$C_p = 0.787\ C_{P_{UO_2}} + 0.205\ C_{P_{ZrO_2}} + 0.008\ C_{P_{FeO}}$$

METALLIC DEBRIS

$$C_p = 0.624\ C_{P_{CS}} + 0.376\ C_{P_{ZIRC}}$$

DISTRIBUTION

U. S. Government Printing Office
Receiving Branch (Attn: NRC Stock)
8610 Cherry Lane
Laurel, MD 20707
275 copies for R4

AEE Winfrith (2)
Dorchester
Dorset
United Kingdom
Attn: R. Potter
P. N. Smith

AERE Harwell
Didcot
Oxfordshire OX11 ORA
United Kingdom
Attn: J. Gittus, AETB

Argonne National Laboratory (3)
9700 Cass Avenue
Argonne, IL 60439
Attn: L. Baker
B. Spencer
D. Cho

Atomic Energy of Canada, Ltd.
Whiteshell Nuclear Research
Establishment
Pinawa, Manitoba ROE1LO, Canada
Attn: D. J. Wren

Battelle Institute e.V. (3)
Am Romerhof 35
D-6000 Frankfurt am Main 90
Federal Republic of Germany
Attn: D. T. Kanzleiter
L. Wolf
K. Fischer

Battelle's Columbus Laboratories (2)
505 King Avenue
Columbus, OH 43201
Attn: F. Cybulskis
R. S. Denning

Brookhaven National Laboratory (4)
Upton, Long Island, NY 11973
Attn: G. A. Green
T. Ginsberg
M. Kahtib-Rahbar
T. Pratt

Professor A. Alonso
Catedra de Tecnologia Nuclear
E.T.S. Ingenieros Industriales
Universidad Politecnica
c/ Jose Gutierrez Abascal, 2
28006-Madrid
Spain

Culham Laboratory
Culham
Abingdom
Oxforshire OX14 3DB
United Kingdom
Attn: F. Briscoe

Division of Nuclear Safety Research (2)
Nuclear Safety Research Center
Tokai Research Establishment
Japan Atomic Energy Research Institute
Tokai, Ibaraki-ken 319-11
Japan
Attn: K. Muramatsu
K. Soda

EG&G Idaho (4)
P. O. Box 1625
Idaho Falls, ID 83415
Attn: C. Allison
P. D. Bayless
K. C. Wagner
R. Gottula

E. I. du Pont de Nemours & Company (3)
Reactor Safety Research Division
Savannah River Laboratory
Building 773-41A
Aiken, SC 29808-0001
Attn: K. O'Kula
D. A. Sharp
G. Marin

ENEA-DISP
DISP/ALCO/PROCS
Via Vitaliano Brancati, 48
00144 Roma, Italy
Attn: M. Colagrossi

Electric Power Research Institute (4)
3412 Hillview Avenue
Palo Alto, CA 94303
Attn: M. Murillo
B. R. Sehgal
E. Fuller
M. Leverett

Energy, Inc.
P.O. Box 736
Idaho Falls, ID 83402
Attn: J. Schroeder

Fauske & Associates, Inc. (2)
6W070 - 83rd Street
Burr Ridge, IL 60521
Attn: M. G. Plys
R. Henry

Wiktor Frid
Statens Vattenfallsverk
Avd. BVK 4
S-16287 Vaellingby
Sweden

General Electric Company
175 Curtner Avenue, MC 766
San Jose, CA 95125
Attn: J. Teng

Gesellschaft fur
Reaktorsicherheit mbH
Postfach 101650
Glockengasse 2
D-5000 Koln 1
Federal Republic of Germany
Attn: J. Langhans

Dan P. Griggs
Engineering Planning
and Management, Inc.
Point West Office Center
Three Speen Street
Framingham, MA 01701

Hanford Engineering Development
Laboratory (2)
Richland, WA 99352
Attn: G. R. Armstrong
L. D. Muhlestein

Joint Research Center (JRC)
21020 ISPRA (Varese), ITALY
Attn: A. Markovina

Kernforschungszentrum Karlsruhe (3)
Postfach 3640
D-7500 Karlsruhe 1
Federal Republic of Germany
Attn: G. Heusener
G. W. Scholtyssek
W. Schoeck

Los Alamos National Laboratory (3)
Los Alamos, NM 87545
Attn: R. J. Henninger
F. Y. Pan
M. Stevenson

Massachusetts Institute of Technology (2)
Cambridge, MA 02139
Attn: M. S. Kazimi
S. D. Clement

Professor M. Mazzini
Departimento di Costruzioni
Meccaniche e Nucleari
Facolta di Ingengneria
via Diotisalvi 2
56100 Pisa, Italy

Netherlands Energy Research
Foundation (ECN)
Postbus 1
1755 ZG Petten
The Netherlands
Attn: H. M. van Rij

OEC
200 Rue de la Loi
1049 Brussels
Belgium
Attn: E. Della-Loggia
SdM2/77

Oak Ridge National Laboratories (6)
P. O. Box Y
Oak Ridge, TN 37830
Attn: S. Greene
S. A. Hodge
A. Malinauskas
C. Hyman
T. S. Kress
M. L. Tobias

Pacific Northwest Laboratory (2)
Battelle Boulevard
Richland, WA 99352
Attn: P. C. Owczarski
C. Wheeler

Philadelphia Electric Company
2301 Market Street
Philadelphia, PA 19101
Attn: G. A. Krueger

Power Authority State of New York
10 Columbus Circle
New York, NY 10019
Attn: R. Deem

Power Reactor and Nuclear Fuel
Development Corporation (2)
Fast Breeder Reactor Development
Project
9-13, 1 Chome, Akasaka
Minato-ku, Tokyo
JAPAN
Attn: T. Aoki
A. Watanabe

Power Reactor and Nuclear Fuel
Development Corporation (3)
Oarai Engineering Center
4002 Narita, Oarai-machi,
Ibaraki-ken, 311-13
Japan
Attn: Y. Himeno
H. Hiroi
O. Miyake

Renssellaer Polytechnic Institute
Department of Nuclear Engineering
Troy, NY 12180-3590
Attn: Prof. R. Lahey

Risk Management Associates
2309 Dietz Farm Road
Albuquerque, NM 87107
Attn: P. Bieniaritz

Science Applications
International Corporation (13)
2109 Air Park Road
Albuquerque, NM 87106
Attn: J. J. Weingardt (10)
P. K. Mast
K. A. Williams
C. N. Amos

Stone & Webster (2)
P. O. Box 2325
Boston, MA 02107
Attn: J. Metcalf
E. Warman

Technische Universitat Munchen
Forschungsgelande
8046 Garching
Republic of Germany
Attn: Prof. Dr. I. H. Karwat

Jack Tills & Associates
P. O. Box 549
Sandia Park, NM 87047
Attn: J. L. Tills
A. Gu

U. S. Department of Energy
Office of Nuclear Safety Coordination
Washington, DC 20545
Attn: R. W. Barber

UKAEA Safety and Reliability Directorate
Culcheth, Wigshaw Lane (6)
Warrington WA3 4NE
Cheshise, United Kingdom
Attn: R. L. D. Young
F. Abbey
P. N. Clough
J. F. Collier
I. H. Dunbar
S. Ramsdale

U. S. Department of Energy
RRT/DOE
NE 530
Washington, DC 20545
Attn: H. Alter

U. S. Department of Energy (2)
Albuquerque Operations Office
P. O. Box 5400
Albuquerque, NM 87185
Attn: J. R. Roeder, Director
Transportation Safeguards
D. L. Krenz, Director
Energy Research Technology
For: C. B. Quinn
R. N. Holton

U. S. Nuclear Regulatory Commission
Division of Reactor System Safety (32)
Office of Nuclear Regulatory Research
Washington, DC 20555
Attn: M. Silberberg
E. Beckjord
G. Burdick
S. B. Burson
L. Chan
M. Cunningham
J. Han
G. Hulman
C. N. Kelber
J. Lane
T. M. Lee
G. Marino

R. Meyer
J. Mitchell
B. Morris
J. Ridgely
D. Ross
T. Speis
T. J. Walker (5)
P. Worthington
R. W. Wright
Z. Rosztoczy

U.S. Nuclear Regulatory Commission (6)
Office of Nuclear Reactor Regulation
Washington, DC 20555
Attn: R. Barrett
V. Benaroya
F. Eltawila
R. L. Palla
C. G. Tinkler
D. D. Yue

University of California at
Los Angeles (2)
Nuclear Energy Laboratory
405 Hilgard Avenue
Los Angeles, CA 90024
Attn: W. Kastenburg
I. Catton

University of Maryland
Department of Nuclear Engineering
College Park, MD 20742
Attn: K. Almenas

University of New Mexico
Department of Chemical
and Nuclear Engineering
Albuquerque, NM 87131
Attn: G. Cooper

University of Wisconsin
Nuclear Engineering Department
Madison, WI 53706
Attn: M. Corradini

Westinghouse Electric Corporation
P. O. Box 355
Pittsburg, PA 15230
Attn: N. Liparulo

Sandia Distribution:

3141 S. A. Landenberger (5)
3151 W. L. Garner
6400 D. L. Hartley
6410 N. R. Ortiz
6412 A. L. Camp
6413 E. D. Bergeron
6413 F. Harper
6415 S. E. Dingman
6415 R. M. Cranwell
6415 J. L. Sprung
6418 J. E. Kelly
6420 J. V. Walker
6421 P. S. Pickard
6422 D. A. Powers
6422 J. E. Brockman
6423 K. O. Reil
6423 R. O. Gauntt
6425 W. J. Camp
6425 R. Gasser
6425 M. Pilch
6427 M. Berman
6427 L. S. Nelson
6429 K. D. Bergeron (10)
6429 D. E. Carroll
6429 F. Gelbard
6429 K. K. Murata
6429 K. E. Washington
6429 D. C. Williams
6440 D. A. Dahlgren
6442 W. A. von Riesemann
6448 D. L. Berry
6450 T. R. Schmidt
6500 A. W. Snyder
6511 L. C. Sanchez
6513 D. D. Carlson
8524 P. W. Dean

NRC FORM 335 (2-84) NRCM 1102, 3201, 3202

U.S. NUCLEAR REGULATORY COMMISSION

BIBLIOGRAPHIC DATA SHEET

SEE INSTRUCTIONS ON THE REVERSE

1 REPORT NUMBER (Assigned by TIDC add Vol. No., if any)
NUREG/CR-5126
SAND88-1407

2 TITLE AND SUBTITLE
TAC2D Studies of Mark I Containment Drywell Shell Melt-Through

3 LEAVE BLANK

4 DATE REPORT COMPLETED
MONTH: May
YEAR: 1988

5 AUTHOR(S)
J. J. Weingardt
K. D. Bergeron

6 DATE REPORT ISSUED
MONTH: August
YEAR: 1988

7 PERFORMING ORGANIZATION NAME AND MAILING ADDRESS (Include Zip Code)
Sandia National Laboratories
Albuquerque, NM 87185

8 PROJECT/TASK/WORK UNIT NUMBER

9 FIN OR GRANT NUMBER
A1198,A1132

10 SPONSORING ORGANIZATION NAME AND MAILING ADDRESS (Include Zip Code)
Division of Reactor Accident Analysis
Office of Nuclear Regulatory Research
U.S. Nuclear Regulatory Commission
Washington, DC 20555

11a TYPE OF REPORT
Technical

b PERIOD COVERED (Inclusive dates)
11/15/87 - 5/15/88

12 SUPPLEMENTARY NOTES

13 ABSTRACT (200 words or less)

A series of parametric calculations of the thermal attack of molten corium on a steel shell has been performed with the TAC2D computer code in order to elucidate uncertainties about the survivability of the BWR Mark I containment boundary in the event of a core-melt accident. Since TAC2D is a two-dimensional heat conduction code, it is not possible to capture some of the complexities of the corium spreading process or the debris-concrete interactions which would occur in this accident scenario. However, the two-dimensional transient nature of the thermal attack is modeled better with TAC2D than is possible with existing debris-concrete interaction codes. This study was therefore undertaken as a supplement to earlier work with debris-concrete interaction codes (like CORCON-MOD2), with the intention of assisting members of expert panels assessing uncertainty in severe accident phenomena for the US Nuclear Regulatory Commission's NUREG-1150 project. A total of 23 calculations are reported, consisting of two base cases (one with overlying water and one without) and numerous sensitivity variations about each case. Sensitivities investigated include mixed versus layered corium, heat transfer parameters upward and downward, initial corium temperature, chemical heating rate, heat transfer conditions in the gap outside the shell, and corium depth.

14 DOCUMENT ANALYSIS - a KEYWORDS/DESCRIPTORS
BWR Mark I; Thermal Analysis; Liner Melting

b IDENTIFIERS/OPEN-ENDED TERMS

15 AVAILABILITY STATEMENT
Unlimited

16 SECURITY CLASSIFICATION
(This page) Unclassified
(This report) Unclassified

17 NUMBER OF PAGES

18 PRICE

*U.S. GOVERNMENT PRINTING OFFICE:1988-202-292:80165

NUREG/CR-5126

TAC2D STUDIES OF MARK I CONTAINMENT DRYWALL SHELL MELT-THROUGH

AUGUST 1988